Eur. J. Mech. B - Fluids 20 (2001) 205–232

S0997-7546(00)01116-X/FLA

Experimental study of chaotic advection regime in a twisted duct flow

Cathy Castelain, Asen Mokrani, Yves Le Guer, Hassan Peerhossaini *

Thermofluids and Complex Flows Research Group, LTI - UMR CNRS 6607, ISITEM, Université de Nantes, La Chantrerie-CP 3023, 44087 Nantes, France

(Received 10 September 1998; revised 30 June 1999 and 29 July 2000; accepted 13 October 2000)

Abstract – The generation of Lagrangian chaos has been studied experimentally in a twisted duct flow, a configuration representing a three-dimensional steady open flow in which various signatures of Lagrangian chaos are documented. The twisted duct consists of four 90° bends of square cross-section; the plane of curvature of each bend is at 90° to that of its neighbors. Dean roll-cells, generated by centrifugal forces and the geometrical perturbation due to the change in curvature plane, are the source of the irregular trajectories of the fluid particles.

The Eulerian nature of the flow was investigated using a laser Doppler velocimeter (LDV). From the Eulerian point of view, the flow is completely regular.

We show by laser-induced fluorescence (LIF) visualization that many characteristics of a Lagrangian chaotic system are present in this flow:

- strong stretching and folding of material lines and surfaces;
- sensitivity to initial conditions;
- exponential growth of stretching in some flow regions.

It is also shown that in some regions of the flow stretchings grow linearly with space, indicating non-chaotic behavior. Due to the chaotic nature of the flow, an equalization of the fly-time of fluid particles was observed during their passage through the twisted duct. © 2001 Éditions scientifiques et médicales Elsevier SAS

Lagrangian chaos / twisted duct flow / laser Doppler velocimeter / laser-induced fluorescence

1. Introduction

The idea of generating ‘spatially chaotic’ behavior from deterministic flow by simple geometrical perturbations has attracted much attention in recent years (Aref [1]; Jones et al. [2]; Le Guer and Peerhossaini [3]). The interest arises both from the very curious fundamental peculiarities of this ‘Lagrangian chaos’ and from the potential of its application in mixing (Saxena and Nigam [4]; Ottino [5]; Villermaux and Hulin [6]; Castelain et al. [7]) and heat transfer (Acharya et al. [8]; Peerhossaini et al. [9]; Mokrani et al. [10]). While temporal chaos has been extensively studied and different scenarios for the transition to turbulence have already been established, Lagrangian chaos, commonly called ‘chaotic advection’, has so far received little attention.

For incompressible two-dimensional steady flows, the equations describing the streamlines define a Hamiltonian dynamical system of one degree of freedom. Time-invariant Hamiltonian systems are conservative and systems of this type are integrable. Particles located between two streamlines at a given time are not transported out of that region by the effect of the flow alone and global mixing in this case can occur only by molecular diffusion. In contrast, if the two-dimensional flow is time-dependent but still non-turbulent,

* Correspondence and reprints.
E-mail address: hp@isitem.univ-nantes.fr (H. Peerhossaini).

the pathlines follow a time-dependent Hamiltonian system that in general is no longer integrable. Mixing is more efficient in these chaotic systems than in their integrable counterparts, since diffusion is now enhanced proportionally to the increased interfacial area generated by advection. In chaotic advection, on the other hand, pathlines of originally neighboring particles diverge exponentially. Such exponential divergence leads in turn to an exponential increase of the interface of the passive scalar, which results in the effective increase in the diffusion constant.

Several highly idealized flows have been considered in order to verify chaotic advection in two-dimensional time-periodic systems (Aref [1]; Khakhar et al. [11]). The chaotic state of the resulting flow was demonstrated not by the calculation of Lyapunov exponents, as is customary for temporal chaos, but by Poincaré maps, which show large chaotic regions (global mixing) for appropriate rotation periods of the vortex filaments.

Steady three-dimensional flows are dynamically similar to two-dimensional time-dependent flows. One can show this equivalence formally by replacing one of the coordinates by a fictitious time. The necessary conditions for the existence of laminar steady three-dimensional flows with chaotic streamlines were pointed out by Arnold [12]. He gave as an example a triply periodic solution of the Euler equation, now known as the ABC flow, which shows a mixing structure similar to that described above. Although this flow cannot be realized in the laboratory, several alternatives capturing its general geometrical features have been proposed as good steady (static) mixers.

The blinking-vortex system (Aref [1]) emulates a ‘closed’ highly idealized two-dimensional chaotic flow. However, it has inspired the construction of a more realistic three-dimensional steady chaotic open flow (Jones et al. [2]; Le Guer and Peerhossaini [3]). Here the rectilinear vortex filaments of the blinking-vortex flow are replaced by a pair of streamwise vortices in a duct flow (called Dean vortices) and the temporal periodicity of the vortices is replaced by the spatial oscillation of a geometrical parameter which is the orientation of the curvature plane. Switching the curvature plane from one bend to another generates a flow that is heuristically equivalent to the flow field of a partitioned-pipe mixer (Khakhar et al. [13]) in which the fluid particles jump from one stream surface to that of the neighboring bend. The flow constructed is a laminar twisted-duct flow made up of a serie of bends (of different cross-sections: circular for Jones et al. [2], square for Le Guer and Peerhossaini [3]). The plane of curvature of each bend makes an angle χ with the curvature plane of the neighboring bends. Parametric studies by Jones et al. [2] in a twisted pipe flow have shown the domain of the rotation angle of the curvature plane for which the Poincaré maps show extended chaotic regions.

Potential technological applications of chaotic advection require an accurate knowledge of the velocity, temperature and concentration fields, of friction factors and of heat transfer coefficients. The unconventional properties and complex basic mechanisms of chaotic mixers themselves warrant a fundamental study. While there is clear evidence of the chaotic advection phenomenon in this special three-dimensional open flow and numerous other examples, the subject is still in need of more laboratory experimentation and verification of its various aspects. A comprehensive review of the state of the art of chaotic advection can be found in Ottino [5].

After the numerical study of Jones et al. [2], based on the simplified Dean model and consequently for small Dean numbers, the purpose of the present work is to investigate ‘experimentally’ the short range and local characteristics of the chaotic advection regime in a twisted-duct flow, ‘for a small number of bends’. Chaotic advection, in such geometries, generates efficient mixing and heat transfer properties, and consequently, allows design of novel continous mixers or heat exchangers operating in laminar regime. The paper is organized as follows: section 2 describes experimental facilities and procedures. In section 3 we present velocity field measurements and show how the flow adjusts itself to variation in the boundary conditions and that the Eulerian field remains predictable. Section 4 is devoted to experimental results on Lagrangian properties of the flow, for a small number of bends. Here we report on the flow visualization by laser-induced fluorescence (LIF) of Lagrangian transport of tracer particles. We show that the flow indeed generates folding

and stretching of material blobs in the same way as observed in two-dimensional periodic chaotic advection. Some dispersion characteristics of the flow are deduced from passive tracer visualization. Finally, section 5 gives some concluding remarks.

2. Experimental facilities and procedures

2.1. Test section

The basic idea here is to generate Dean roll-cells in a sequence of bends in which the curvature plane of each bend makes an angle χ with that of its neighboring bend. Each bend is a 90° curved duct of square cross-section of 40 ± 0.02 mm sides (a). The radii of the inner and outer curved surfaces are respectively $R_i = 200$ mm and $R_o = 240$ mm (curvature ratio $\beta = R_c/a = 5.5$). The bends are machined out of a block of transparent Plexiglas. The small radius of curvature was chosen to provide a strong radial pressure gradient across the bend and thus promote the rapid development of Dean roll-cell structure. A numerically controlled milling machine was used to fabricate all bends to precise dimensions (± 0.02 mm); this precision ensures the absence of unmatched joints between successive sections. The bends are then polished by hand. Careful attention was paid to component finishing to ensure uniform geometry.

Each two successive bends are separated by a straight duct section of 276 mm in order to decouple roll-cell formation in the successive bends. The straight ducts are also appropriate places for LDV measurements One of the straight ducts is also instrumented by tracer injectors. A schematic diagram of the test section is shown in *figure 1*.

Because of the square cross-section, the angle between the plane of curvature of two successive bends χ can vary in multiples of $\pi/2$. From a phenomenological argument, we have found that the most favorable angle χ for generating irregular trajectories is $\pi/2$. Though the square geometry of the cross-section does not allow verification of the effect of a large number of possibilities for χ, the numerical results of Jones et al. [2] and Le Guer [14] suggest that $\chi = \pi/2$ is in fact the optimal angle for efficient stirring in twisted pipes of circular cross-section. We presume that the same is valid in ducts with square cross-section as well.

2.2. Water tunnel facility

A water tunnel facility was specifically designed and constructed in order to provide a well controlled flow through the test section. The test facility, an open loop tunnel, is shown schematically in *figure 2*. When the tunnel operates with water, the pressure head is provided by a constant-elevation reservoir of 256-liter capacity to assure stable flow. The flow generated passes through a series of development elements before entering the test section. It first enters a 4° half-angle diffuser specifically designed to prevent flow separation. The fluid then passes through a settling chamber of 120 mm $\times$ 120 mm cross-section and 160 mm length, and then through a 1-to-6.5 section ratio nozzle; a three-dimensional nozzle whose sides are profiled to follow polynomials of third degree. A 2000 mm metallic straight duct is provided at the exit from the nozzle for relaxation of the flow streamlines and development of Poiseuille flow. In order to verify the characteristics of the flow before entering the test section, a transparent straight duct of 800 mm is fitted between the straight metallic section and the twisted duct to probe the entering flow by LDV. The total length of the straight section is 70 times the hydraulic diameter, which ensures fully developed Poiseuille flow at the entrance to the first bend. The test section (twisted duct) is followed by a transparent straight duct in which the effect of the successive bends on mixing can be examined.

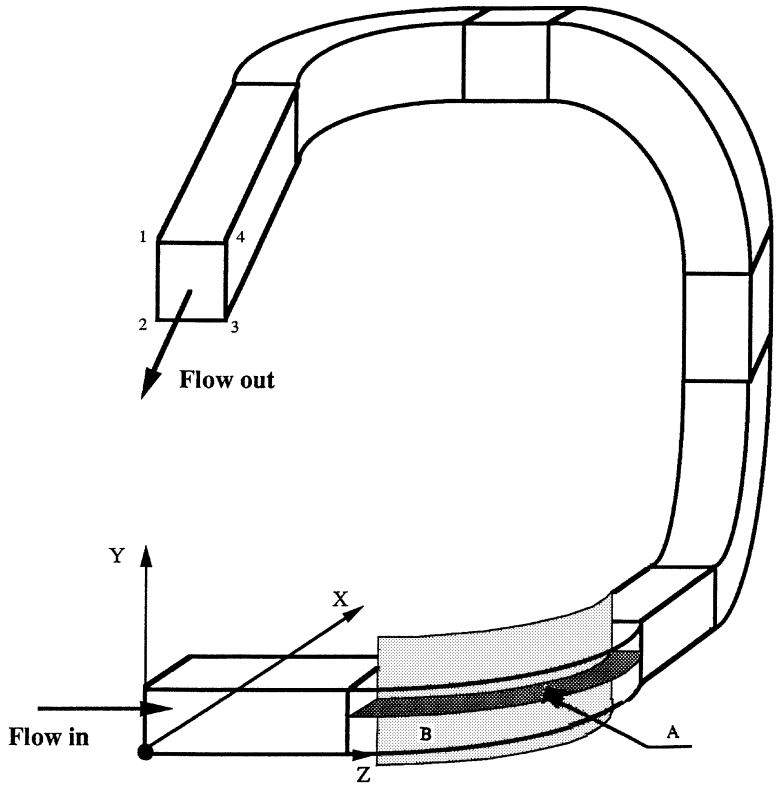

Figure 1. Twisted duct test section consisting of four bends. This is one of several possible test section configurations.

The flow rate through the tunnel is measured by an electromagnetic flowmeter (Rosemount 8711R with transmitter 8712) installed just upstream of the diffuser. When the flow speed is less than 300 mm/s, the accuracy of the flowmeter is within 1%. The temperature of the working fluid is controlled by a heat exchanger located immediately downstream of the constant-level reservoir.

2.3. Flow visualization and laser Doppler velocimetry

Flow visualization by laser-induced fluorescence (LIF) technique is used in this experiment. The flow is illuminated by a blue laser light at a wavelength of 488 nm; the re-emitted light is green, of about 514 nm

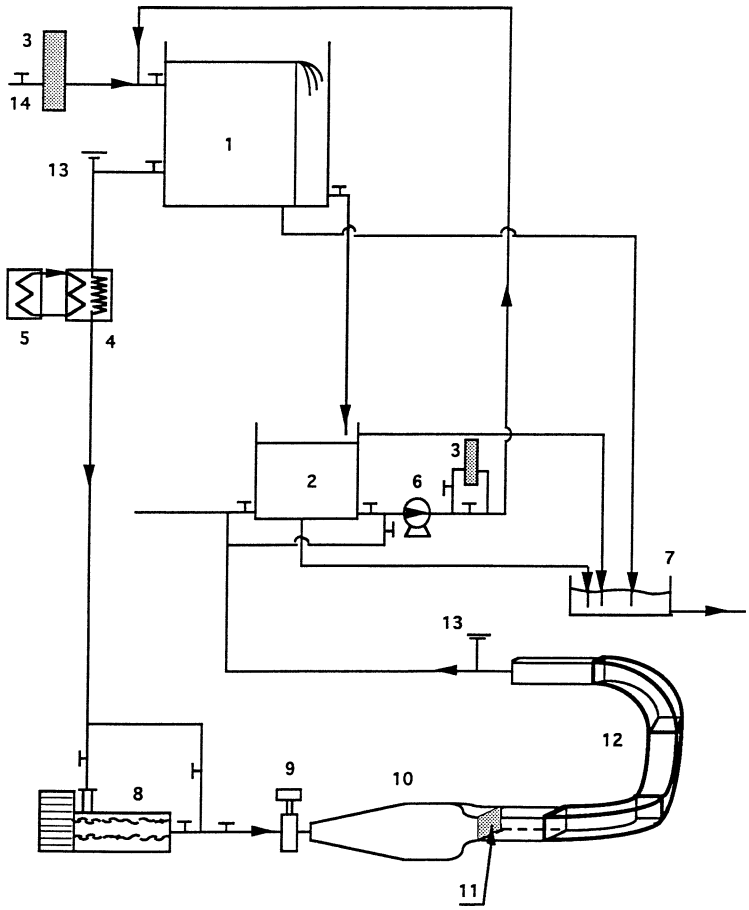

Figure 2. Schematic diagram of the water tunnel facility: 1 – constant-elevation reservoir, 2 – return tank, 3 – filter set, 4 and 5 – heat exchanger, 6 – pump, 7 – drain, 8 – pump, 9 – electromagnetic flowmeter, 10 – diffuser and settling chamber, 11 – nozzle, 12 – test section, 13 – valve, 14 – valve.

wavelength. We used a 5 watt argon ion laser source to illuminate the flow cross-section. An aqueous solution of fluorescein is introduced to the flow from an elevated reservoir through a special dye circuit. A cooling-heat exchanger set, whose temperature is controlled by the signal from the working fluid temperature, is used to bring the temperature of the tracer close to that of the working fluid. Fluorescein solutions of mass concentration 1 mgr/l were used, so that density variation of the working fluid due to tracer addition is negligible. The tracer flow rate is adjusted by means of small high-precision valves that control dye delivery to each injection point so that it does not perturb the flow. In this experiment, dye can be injected by three methods:

– in the first method, called point injection, the injector device is a hypodermic needle of 0.25 mm outer diameter, fixed at the tip of a bent tube. The injector assembly can move by micrometric displacement mechanisms in two transverse directions in the tunnel cross-section. In this manner the whole duct cross-section can be scanned. The injector set is fixed at 170 mm from the entrance of the straight duct that precedes the first bend. In point injection, each injector marks a streakline in the flow. As the flow is steady, each dye streak marks a trajectory and one can follow the transverse stretching and deformation of the cross-section of each trajectory as it passes through different bends;
– in the second method of injection, a thin film of tracer is introduced into the flow through a porous metallic strip mounted flush with the side wall of a short straight duct. The basic design of this injector

has been described elsewhere (Peerhossaini and Wesfreid [15]). In this manner we can track the motion and deformation of a fluid film in the wall region. By changing the orientation of the straight duct, tracer can be injected on any of the four walls of the test section. The injection is made at 70 mm upstream the entrance to the first bend;

– in the third method, the tracer is injected with a syringe upstream of the settling chamber; the tracer is distributed in the whole section. This kind of injection allows overall visualization of the Dean roll-cells.

The cross-sections of the flow are viewed by a charged coupled device (CCD) camera (SONY DXC 101 P) equipped with a zoom lens. It is crucial that images taken in different streamwise sections of the flow be totally comparable from orientation and optical points of view. For this purpose, a traversing mechanism was constructed in which the relative position of the camera and the laser light sheet is fixed. The traversing mechanism rotates around the center of curvature of the bend under investigation and scans the flow at different angular positions. *Figure 3* shows the traversing mechanism and the camera orientation for viewing the illuminated plane at approximately a 90° angle relative to the light sheet. A plexiglas lens corrects the optical deformation of the images due to the surface curvature. A fluid of refraction index close to that of Plexiglas is injected between the lens surface and the bend outer wall to compensate for the material changes in the optical path. A differential filter in front of the camera eliminates the unabsorbed incident laser light, and a biconvex lens after cylindrical lens ensures a thin laser sheet.

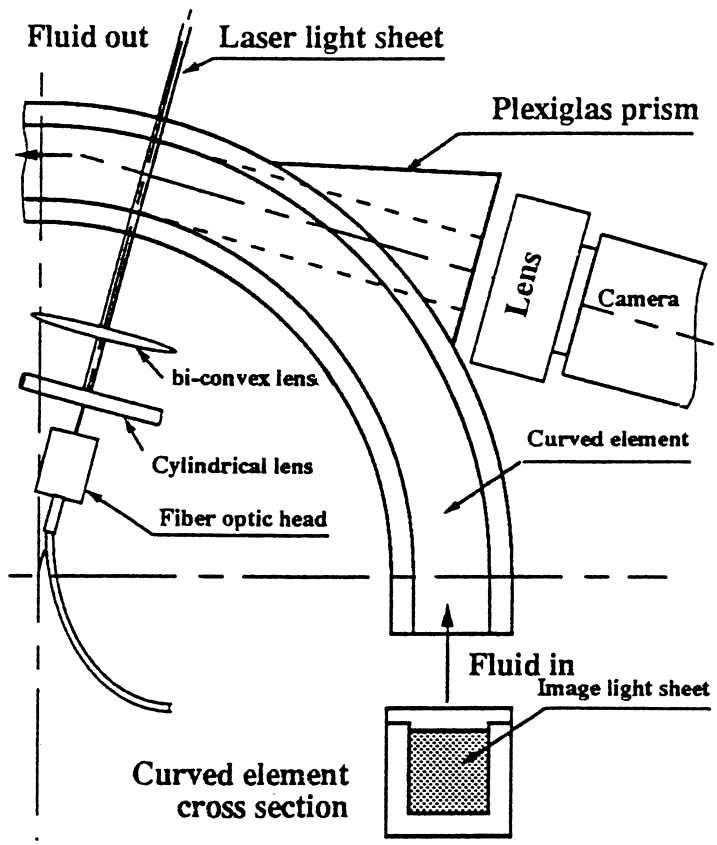

Figure 3. Displacement mechanism for LIF visualization and image acquisition in the curved ducts.

Images viewed by the camera are visualized on a monitor screen and recorded by a video recorder. The same images are transferred directly to a digital image-processing system where they can be recorded and analyzed by the aid of a small computer. This provides a very flexible combination for qualitative and quantitative analysis of the transverse motion of a passive tracer in the test section.

The streamwise velocity is measured by a laser Doppler velocimeter (LDV). Translation of the measuring volume, data acquisition and data analysis are performed by an autonomous computer.

3. Flow characterization

Since the Lagrangian chaos is generated by perturbation of the velocity field, the question arises of the extent to which the local or Eulerian field is affected by the curvature plane change.

In order to study the Eulerian characteristics of the flow, detailed velocity measurement and flow visualization experiments were performed in all bends.

3.1. Analysis of the Dean flow

In laminar flow through ducts, the effect of even very slight curvature is not negligible. Streamline curvature causes a secondary flow to appear that consists of a pair of counter-rotating roll-cells when viewed in the duct cross-section. The roll-cells are called Dean roll-cells after W.R. Dean [16], who developed a theory of this secondary flow phenomenon. We thus call the flow of fluid in a curved duct Dean flow and the corresponding control parameter the Dean number, defined as:

$$Dn = \left(\frac{Wa}{\nu}\right)\left(\frac{a}{R_c}\right)^{1/2}. \tag{1}$$

Here W is the mean velocity, ν the kinematic viscosity, a is the duct width and R_c the radius of curvature. The plane separating two Dean roll-cells (the symmetry plane) is parallel to the curvature plane of the bend.

Velocity measurements were made in the straight duct upstream of the first bend to determine whether the flow is fully developed. The profile of the axial velocity is measured 205 mm upstream of the entrance to the first bend to avoid the upstream effects of Dean roll-cells. Measurements by Humphrey et al. [17] and the full Navier–Stokes calculations of Duchêne et al. [18] have shown that velocity profiles within five hydraulic diameters upstream of the curved duct are affected by centrifugal force.

Figure 4 shows the axial velocity across the duct width at various Dean numbers. Axial velocity w is normalized by the bulk velocity W and distances are normalized by the duct width a. *Figure 4* shows that up to $Dn = 389$, the velocity profiles follow a 'parabolic' distribution, with maximum velocity at the channel center. For Dean numbers higher than 389, the velocity profiles become flatter in the center and more accelerated close to the walls. Since the main aim of this study is to investigate the emergence of a spatially chaotic regime from a laminar duct flow, we restrict attention to the flows with maximum Dean numbers of 530, below which the flow may be considered laminar.

Flow leaving the straight section enters the first bend, a 90° curved duct with its curvature plane horizontal. As the downstream evolution of the chaotic advection flow depends on the initial conditions, we first analyze in detail the flow regime as it emerges from the first bend. To this end it is attempted first to characterize the Dean roll-cells generated in this section and to compare them with those of the classical curved-duct flow. Then the complexities that arise from the rotation of curvature plane are addressed.

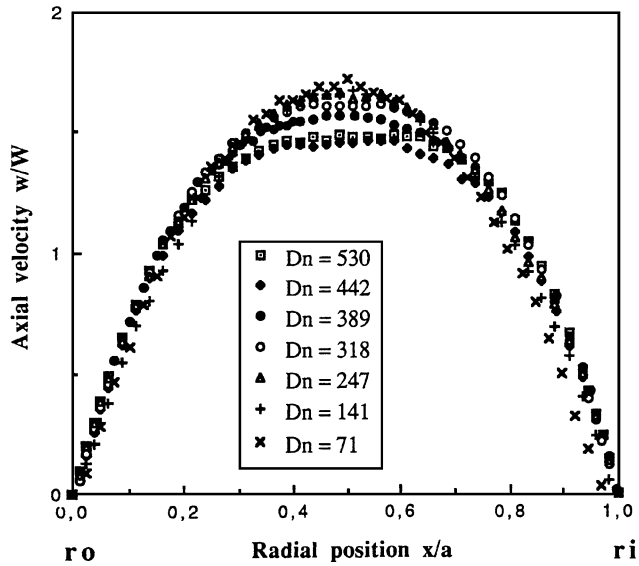

Figure 4. Axial velocity profiles across the channel span in the straight duct upstream of first bend.

Axial velocity was measured in the plane of curvature of the curved duct. Velocity measurements in the curvature plane are carried out in the midspan and the profiles there, called 'symmetry plane profiles', span the channel from concave wall to the convex wall. In these profiles, the origin of coordinates (0 mm) corresponds to the concave or outer radius wall and the abscissa 40 mm coincides with the convex or inner radius wall. Parallel to the velocity measurements, the flow structure was also visualized by LIF for different Dean numbers and at every 15° angular position in the first bend. *Figure 5* shows the flow structure at the entrance, middle and exit from the first bend for Dean numbers of 141 and 352. These roll-cell structures began to take shape at 45° and have developed completely at the exit from the first bend. The velocity profiles in *figure 6* show the generic characteristics of Dean flow-velocity profiles measured in the symmetry plane: the maximum velocity is shifted from the duct center towards the outer concave wall, a shift due to the effect of secondary flow that appears in the form of a pair of roll-cells. The higher the Dean number, the closer the maximum axial velocity $w_{\max}$ is to the concave wall. At $Dn = 141$ the location of the maximum axial velocity, $w_{\max}$, occurs at $x_m/a = 0.38$, while for $Dn = 530$ the maximum is at $x_m/a = 0.22$. *Figure 6* shows that the central parts of the velocity profiles are deflected more inwards at higher Dean numbers. This observation supports the idea that the Dean roll-cells are still in their developing stage and have not yet reached the axially invariant state. In their early stages of development, the central part of the velocity profiles gradually bends inwards as the Dean number increases. After reaching a maximum deflection (overshoot position), they undergo a reverse outward bending as the Dean number increases. They eventually reach an equilibrium state in which they no longer change with Dean number. Details of the processes preceding the axially invariant state are addressed in the numerical work of Soh [19] and the experimental work of Hille et al. [20]. Experimental results of Hille et al. [20] show that for $Dn = 228$ ($R_c/a = 6.45$), the axially invariant state is reached at an angular position of $\theta = 108°$ from the bend entrance. We recall that in the present work, R_c/a is 5.5. Soh [19] has found that the progressive movement of the maximum axial velocity $w_{\max}$ towards the concave wall continues up to $\theta = 44°$. At this angle the maximum velocity occurs at $x_m/a = 0.15$, close to the concave radius wall. In the course of this development, the value of $w_{\max}$ in the midplane decreases with streamwise distance. In the downstream region, the position of maximum axial velocity $w_{\max}$ moves gradually inside towards the channel center, while its value continues to decrease.

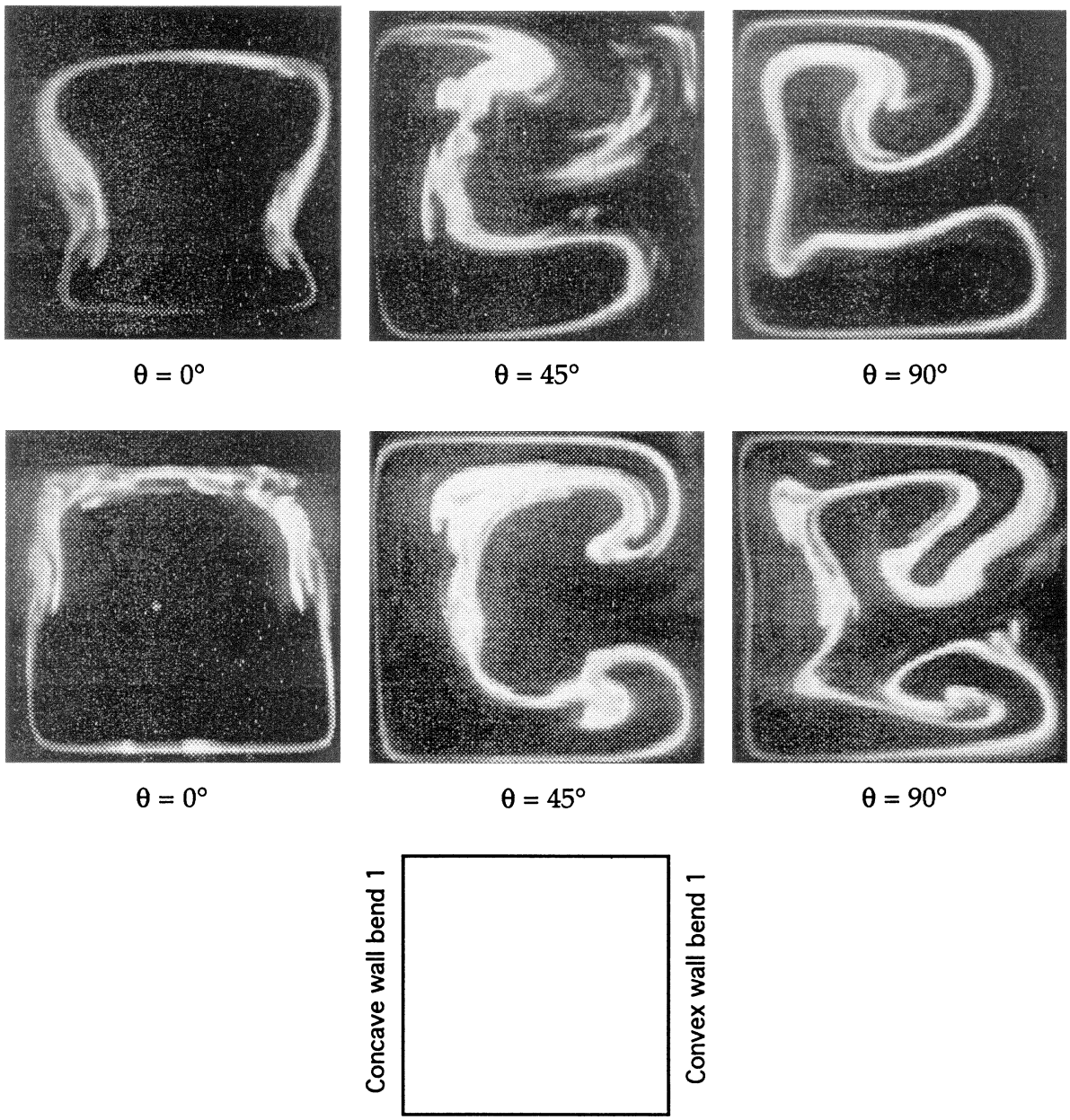

Figure 5. Flow visualization at $\theta = 0°$, 45° and 90° in first bend; top: $Dn = 141$; lower $Dn = 354$.

In the axially invariant regime, which appears at $\theta = 99.3°$, Soh [19] has found $w_{\max}$ to occur at a distance x_m from the concave wall that is a quarter of the total span.

3.2. Twisted curved duct flow

The flow passes through the first bend and enters the second bend, whose plane of curvature is perpendicular to that of the first bend. *Figure 7* shows axial velocity profiles in the plane perpendicular to the symmetry

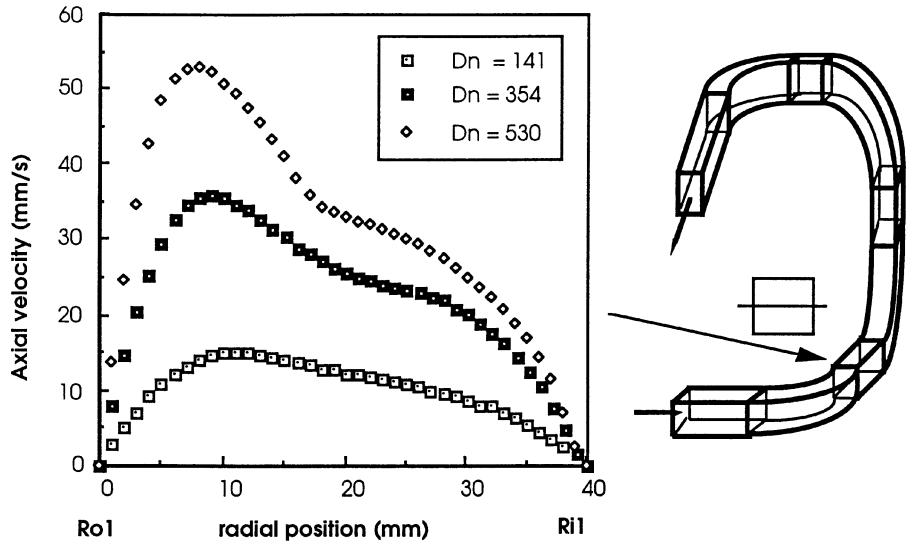

Figure 6. Axial velocity profiles in the symmetry plane at exit from first bend.

plane of the roll-cells (of the first bend), measured at the entrance to the second bend for different Dean numbers. Corresponding flow visualization images are also shown on this figure. The maximum velocity is shifted towards the flat wall of the second bend, which is in the continuity of the concave wall (R_{o1}) of the first bend. The visualized structures show the same phenomenon: Dean roll-cells are oriented in the same direction as in the first bend. Therefore, the curvature plane switch has had no immediate effect. At angular position 30°, the roll-cells start to reorient themselves according to the direction of the centrifugal force in the second bend. *Figure 8* shows the visualized flow and measured velocity profiles in this section.

The reorientation of the roll-cells is strengthened in the rest of the second bend. At the exit from the second bend shown in *figure 9*, roll-cells have rotated completely and are oriented according to the boundary conditions of the second bend. For low Dean number case ($Dn = 141$), this orientation has already achieved the invariant state, while for higher Dean numbers ($Dn = 354$ and 530), the process is not yet completed.

The flow in the third bend was also investigated by measuring velocity profiles in a plane perpendicular to the symmetry plane and visualizing the formation of Dean roll-cells for Dean numbers ranging from 141 to 530. *Figure 10* shows the Dean roll-cells at the entrance to the third bend. They still follow the rotation protocol of the second bend. Velocity profiles at the entrance to this section are also shown in *figure 10*. The eccentric form of the profiles confirms the visualization results: they are still under the influence of the centrifugal force of the second bend. Reorientation of the roll-cells follows the same process as in the second bend: at 30° the roll-cells start to reorient themselves to the direction of the centrifugal force in the third bend. At the exit from this bend, as shown in *figure 11*, the Dean roll-cells are almost completely redeveloped.

Flow visualization in the fourth bend (*figure 12*) for $Dn = 141$ and 530) shows the progressive reorientation of the flow structure in this bend. Unlike the previous bends, the Dean roll-cells are already perturbed at the entrance to the bend. At the exit, however, they are well developed according to the rotation protocol in this bend.

At every step change in the curvature plane, there are two opposite choices for rotation of the curvature plane for the next bend. Depending on the choice, one can either continuously squeeze one roll-cell and enlarge the other, or periodically squeeze and enlarge one roll-cell while doing the opposite to the other one. In the former process, one can probably make one cell disappear after enough step changes, and the flow will be transformed

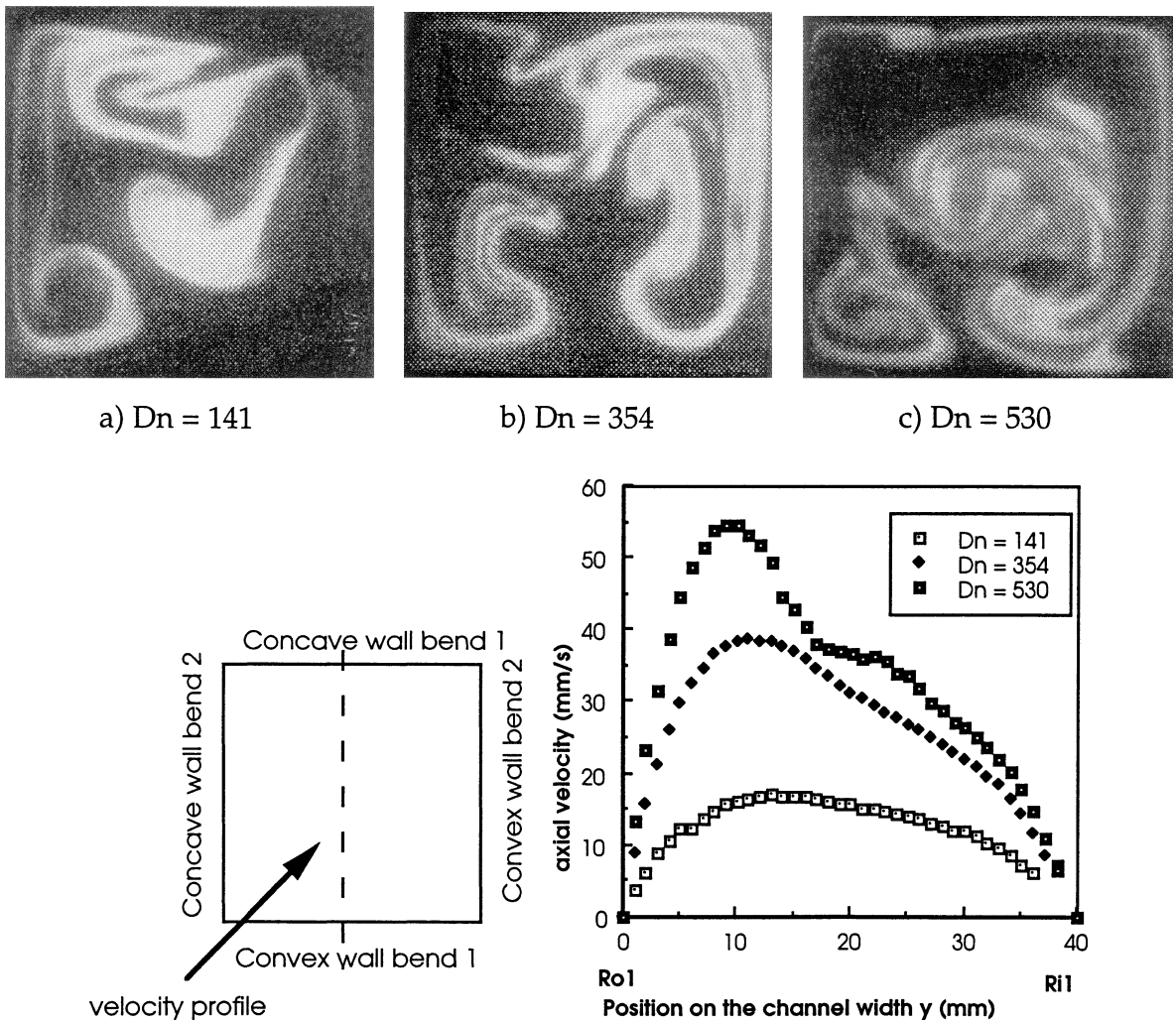

Figure 7. Axial velocity profiles in the plane perpendicular to the symmetry plane of second bend at entrance to this bend, and flow visualization for different Dean numbers at $\theta = 0°$ in the second bend.

to a single-cell flow or a swirl. This process is much faster at high Dean numbers, and has probably occurred in the vortex coalescence observed in previous experiments. In the present experiment, however, a pair of distinct roll-cells is always present in the flow at the exit section.

4. Flow visualization results

4.1. Qualitative characterization of chaos

Here are presented the key results of experimental assessment of chaos in twisted-duct flow. Unlike previous numerical studies, the experimental assessment of chaos in this three-dimensional flow is largely qualitative. In other words, we do not identify horseshoe maps, Poincaré sections, etc. The qualitative nature of the results, however, poses no serious difficulties, since the distinction between the regular and chaotic regimes is easily

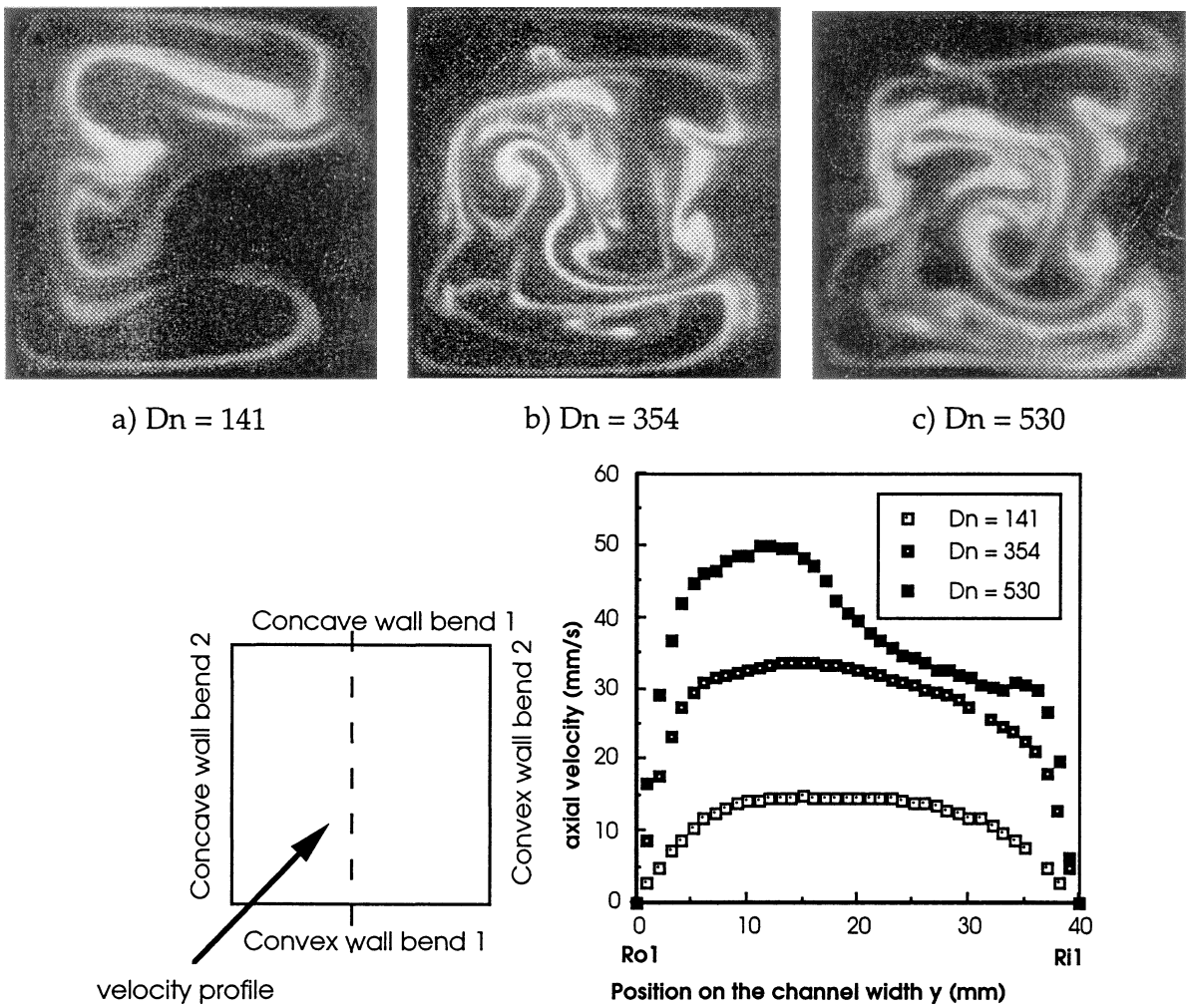

Figure 8. Axial velocity profiles in the plane perpendicular to the symmetry plane of second bend at $\theta = 30°$ in the second bend and flow visualization for different Dean numbers at $\theta = 30°$ in the second bend.

made: the strong transverse stretching and folding that appears in the chaotic behavior readily distinguishes this state from the regular state.

A system can be classified as chaotic if it satisfies any of the following criteria, although they are not completely equivalent (Doherty and Ottino [21]):

- sensitivity to initial conditions (Lyapunov exponents);
- production of a horseshoe map characterized by the kinematic mechanisms of stretching and folding;
- production of transverse homoclinic or heteroclinic intersections.

The term ‘stretching’ implies deformation of the material in the direction of the streamlines, while ‘folding’aligns them across the streamlines.

In what follows, experimental evidence is given for the existence of zones of irregular regime in a twisted duct composed of four bends.

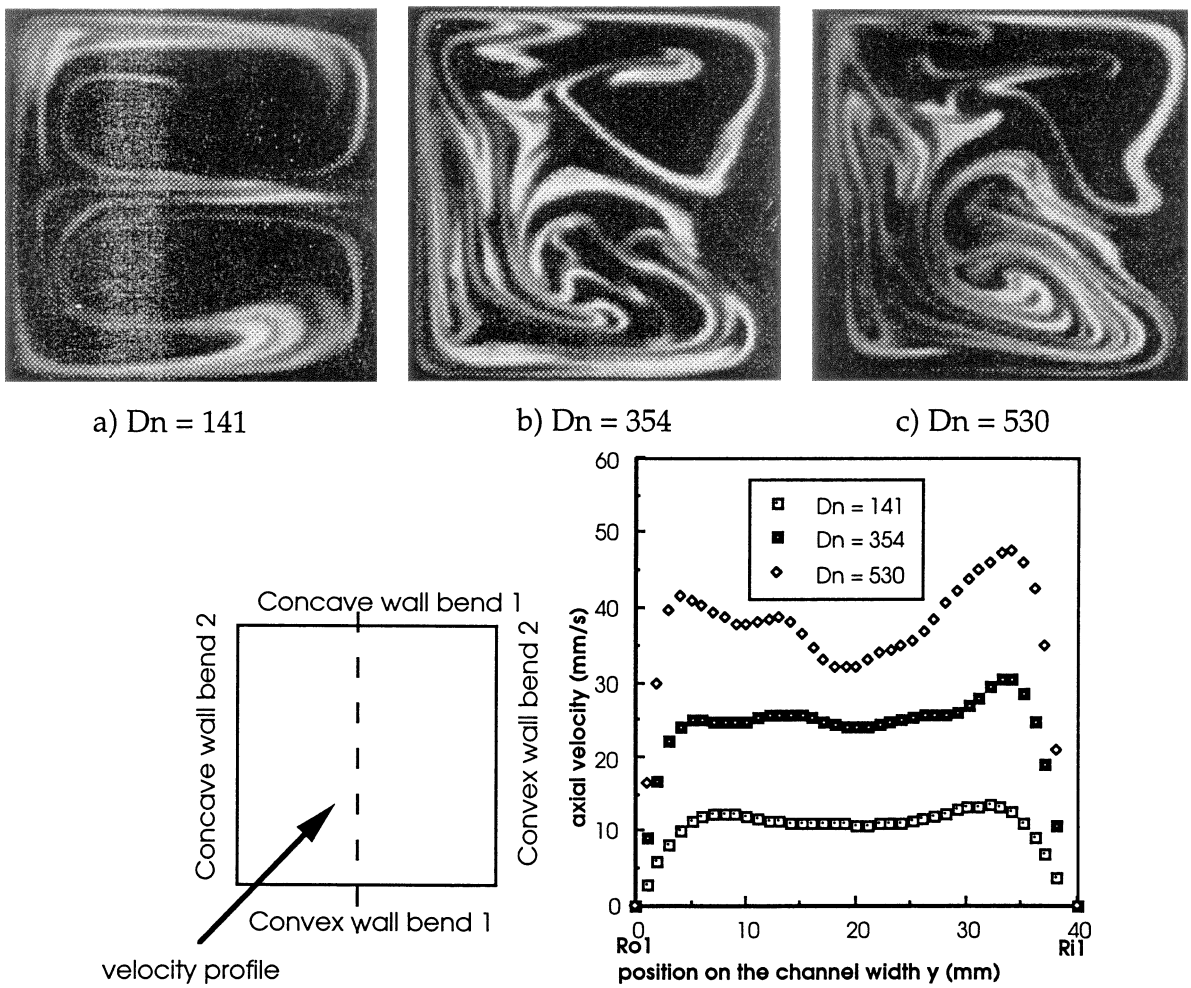

Figure 9. Axial velocity profiles in the plane perpendicular to the symmetry plane of second bend at exit from the second bend and flow visualization for different Dean numbers at $\theta = 90°$ in the second bend.

4.1.1. Whole field observations

By tagging fluid blobs with a tracer, the phase-space (which is here the same as physical-space) evolution of the trajectory of a family of fluid particles has been observed. The type of deformation of such blobs reveals the chaotic or regular nature of the flow.

LIF visualizations show evidence of extensive transverse folding and stretching of fluid elements in the twisted duct flow. It is of interest to study the complexity of the structures arising from the continuous stretching and reorientation of labeled fluid elements. In a simple curved-duct or helicoidally coiled-tube flow (non-chaotic), they would have attained a regular Dean roll-cell pattern.

A very thin film of tracer (fluorescein solution) is injected, through the side wall of the straight duct preceding the first bend, onto the straight duct wall corresponding to the convex wall of the first bend. Its evolution is then followed through the twisted duct. For Dean numbers $Dn = 389$, *figure 13* follows the dyed film as it passes the 45°, 60°, 75° and 90° angular positions from the entrance of the fourth bend. Focusing on fluid element A in *figure 13(a)*, we see that between 45° and 60°, it rotates from a vertical to a horizontal position. Other parts

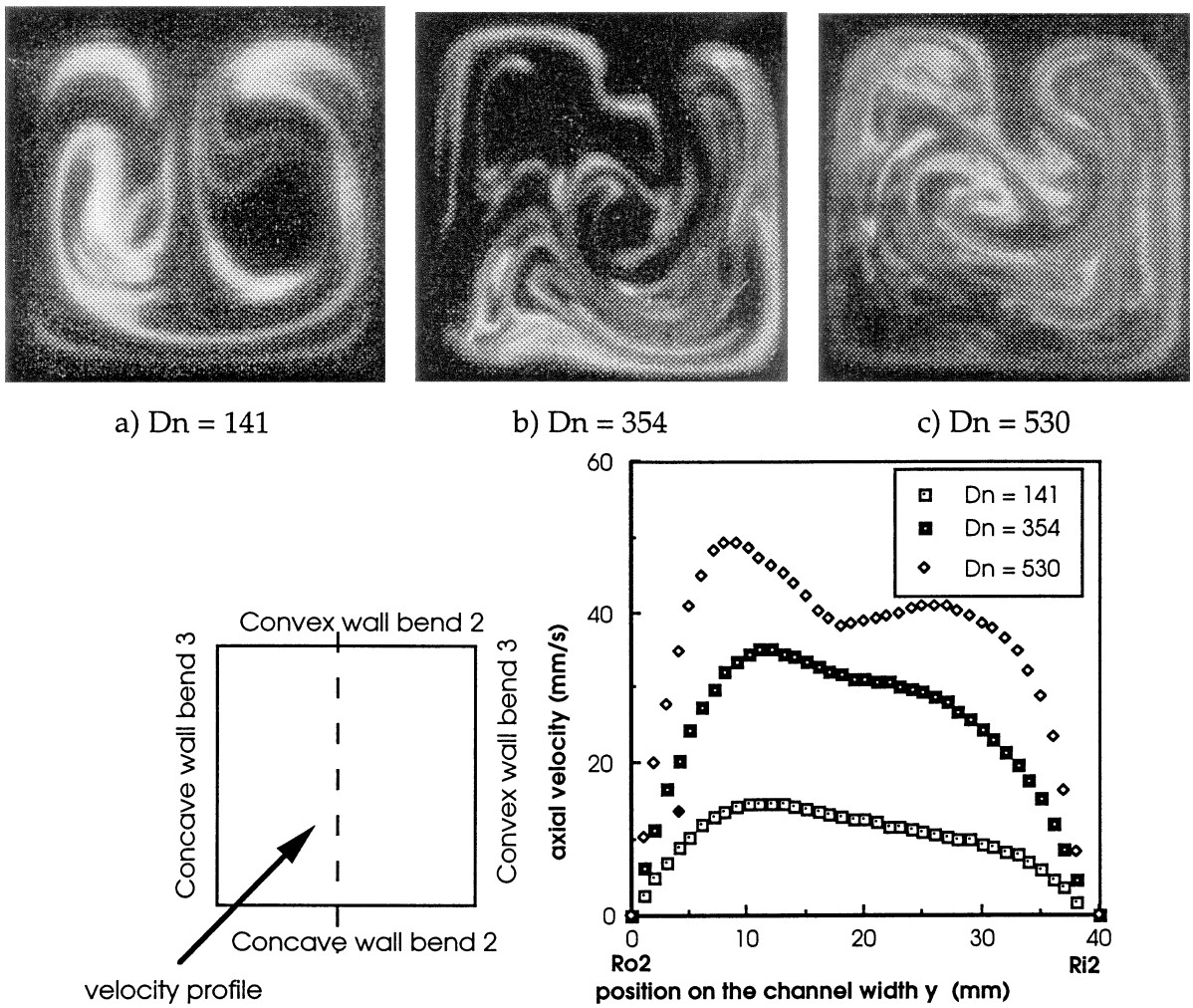

Figure 10. Axial velocity profiles in the plane perpendicular to the symmetry plane of third bend at the entrance to this bend and flow visualization for different Dean numbers at $\theta = 0^\circ$ in the third bend.

of the dyed fluid have also rotated in this interval. Dean roll-cells in this flow produce elliptic orbits with the cell center as an elliptic point. *Figure 13* in fact shows the deformation of material lines under the effect of an elliptic point.

In order to visualize the stretching and folding of material lines in the bulk flow, in another set of experiments a small dye injector was progressively displaced vertically through the center line of the first bent cross-section. The dye injector was placed at 170 mm from the entrance to the first bend. Forty uniformly distributed points along the vertical line were labeled in this manner. *Figures 14(a), (b)* show images of the dyed line at the exit from the first and the exit from the fourth bend, respectively, for $Dn = 247$. Comparison of the two images shows that the regular pattern of Dean roll-cell streamlines has been totally destroyed at the exit from the fourth bend by the curvature switch in the three bends downstream of the first bend.

In fact, the dye injected at 40 discrete points along the line has spread over a large cross-sectional area, showing strong stretching and dispersion at the exit from the fourth bend.

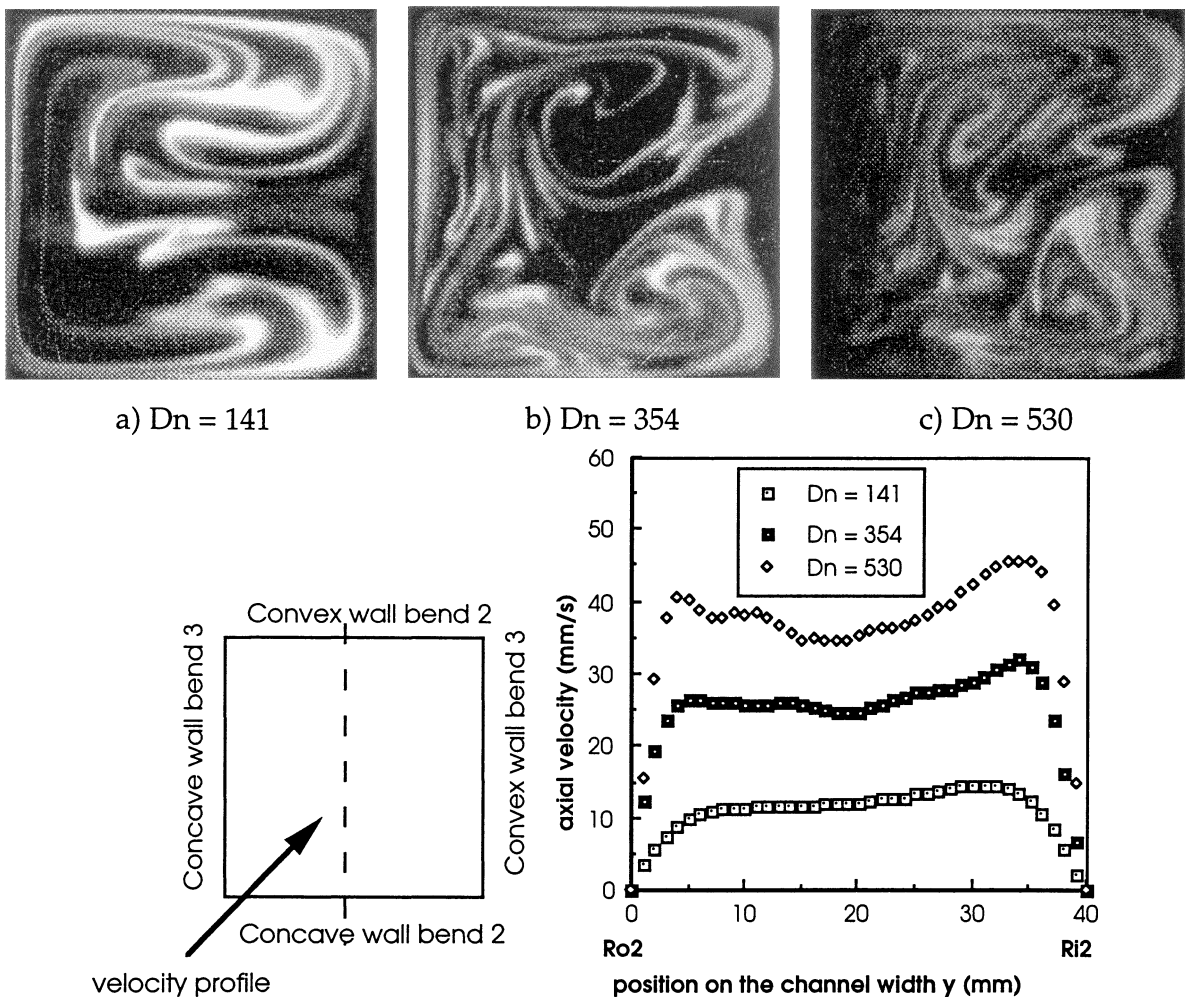

Figure 11. Axial velocity profiles in the plane perpendicular to the symmetry plane of third bend at the exit from the third bend and flow visualization for different Dean numbers at $\theta = 90°$ in the third bend.

This spreading could have been even larger had we initially distributed the dyed fluid elements more uniformly at the inlet of the twisted duct. In order to examine the extent of this enhancement, 81 points were labeled and distributed uniformly in the duct cross-section (as shown in *figure 13*) 170 mm upstream of the entrance to the first bend. *Figure 14(c)* shows the image at the exit from the fourth bend.

The flow-visualization images shown above demonstrate qualitatively that four bends with different planes of curvature are sufficient to cause considerable stretching and folding in a steady laminar duct flow. The spreading of dyed fluid is a fingerprint of drastically diverging trajectories of fluid particles initially close together. The spreading is effected by the stretching and folding in physical space.

4.1.2. Regular and chaotic zones

Chaotic advection is generated by introducing an angle between the curvature planes of two successive bends. If this angle (geometric perturbation) is 0° or 180°, the dynamical system of equations governing the trajectories of the fluid particles is integrable and hence the flow regime is regular. However, if the angle is different from 0°

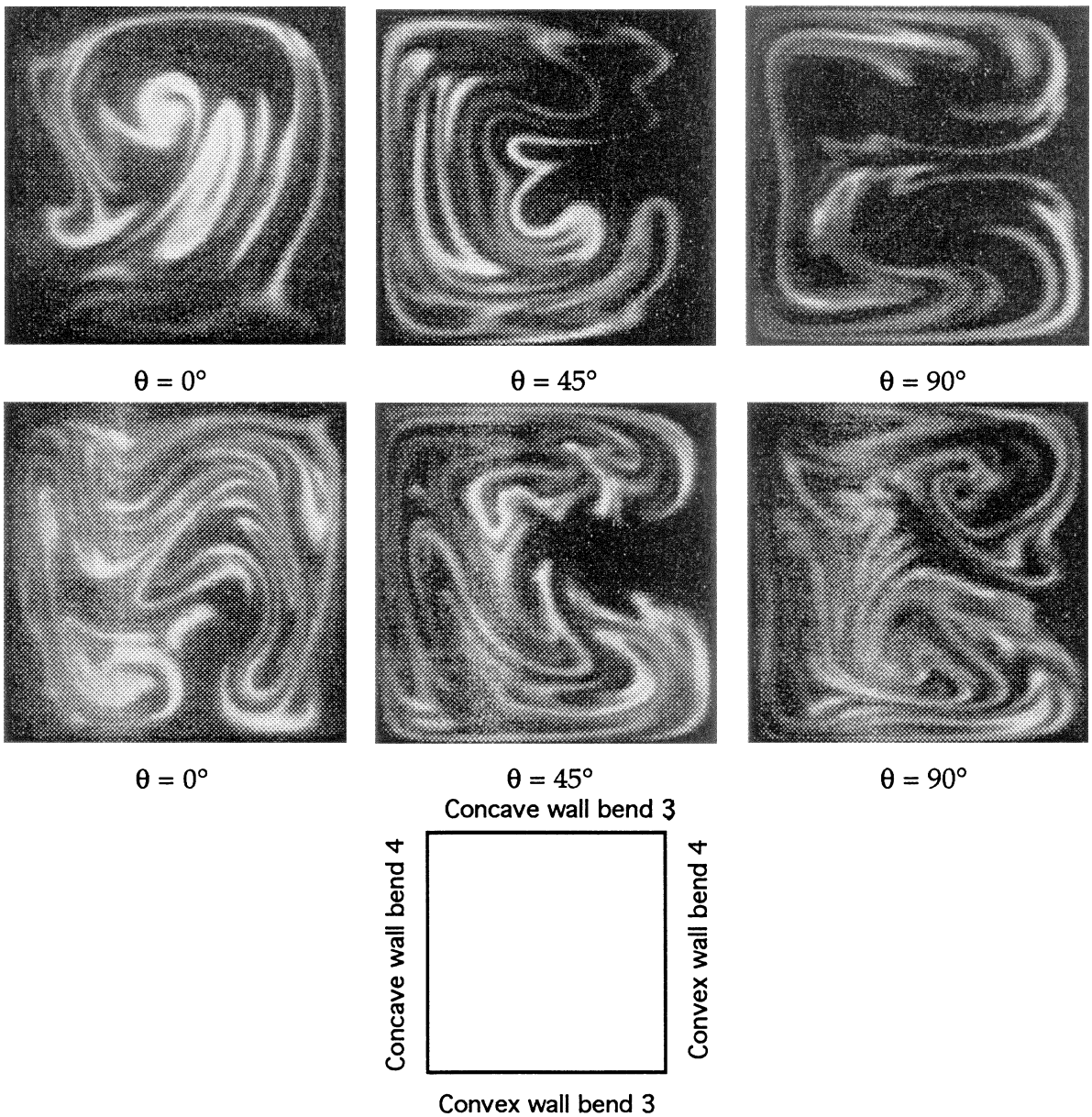

Figure 12. Flow visualization at $\theta = 0^\circ$, 45° and 90° in fourth bend; top: $Dn = 141$; lower: $Dn = 354$.

or 180°, the system is non-integrable, chaotic and the fluid particles follow irregular trajectories. The adjective chaotic implies one of the following properties:

- sensitivity to initial conditions;
- production of stretching and folding;
- production of transverse homoclinic or heteroclinic intersections.

In practice, it is not possible to show experimentally the third property above. The first two properties are the subject of experimental demonstration in this work. If the geometric perturbation is small, certain flow tubes remain regular and retain regular trajectories while the other trajectories entangle and become chaotic zones;

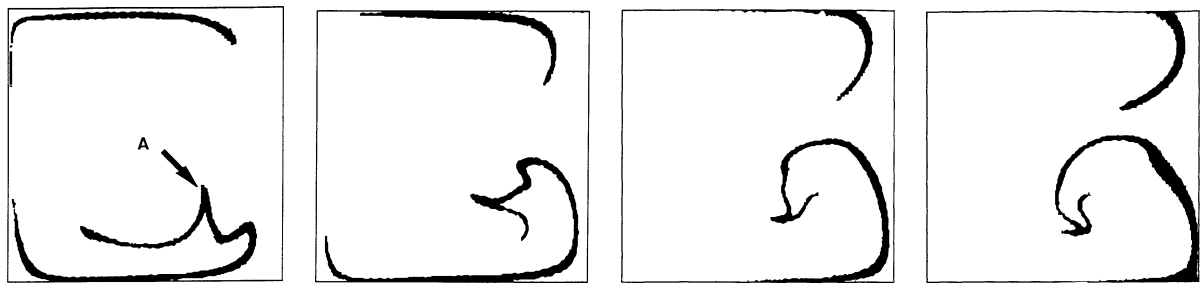

Figure 13. Stretching and reorientation of a dyed fluid surface as it passes at angular positions: (a) $\theta = 45°$; (b) $\theta = 60°$; (c) $\theta = 75°$; (d) $\theta = 90°$ in the fourth bend.

Figure 14. Stretching and folding of a fluid line marked at 170 mm upstream of the entrance to first bend cross-section: (a) image of the flow cross-section at exit from the first bend of 40 uniformly distributed marked points on the vertical center line at the entrance to the first bend; (b) image at the exit from the fourth bend of the points in (a); (c) image at the exit from the fourth bend of 81 marked points uniformly distributed at the entrance to the first bend.

the regime is then called ‘mixed’. The flow domain occupied by regular regions decreases when the angle between the curvature planes of the successive bends approaches 90° or when the number of bends increases.

To give a qualitative indication of the existence of the mixed regime, the fly-times at the exit from the fourth bend were measured for forty points each consisting of an ensemble of fluid particles (labeled by tracer), initially arranged on a line from the top of the first bend cross-section to the bottom and passing through the centers of the two Dean roll-cells. The fly-time is measured for each labeled ensemble of fluid particles at the exit from the first, second, third and fourth bends. *Figures 15(a), (b)* plot the fly-time as a function of the initial position of the ensemble of fluid elements at the entrance to the first bend, for Dean numbers 141 and 352, respectively. The figures show that fly-times are constant at the exit from the first bend, since the time is too short for the effect of Dean roll-cells on the fluid trajectories to appear. Close to the walls, the long fly-times show the wall effect. At the exit from the successive bends, the curves show zones of long fly-time surrounded by zones of almost constant fly-time. The long-fly-time areas are attributed to the irregular (chaotic) zones in which fluid particles have visited a large number of positions in the duct cross-section, so that their fly-time is greater than those of fluid particles that have traveled along the core flow.

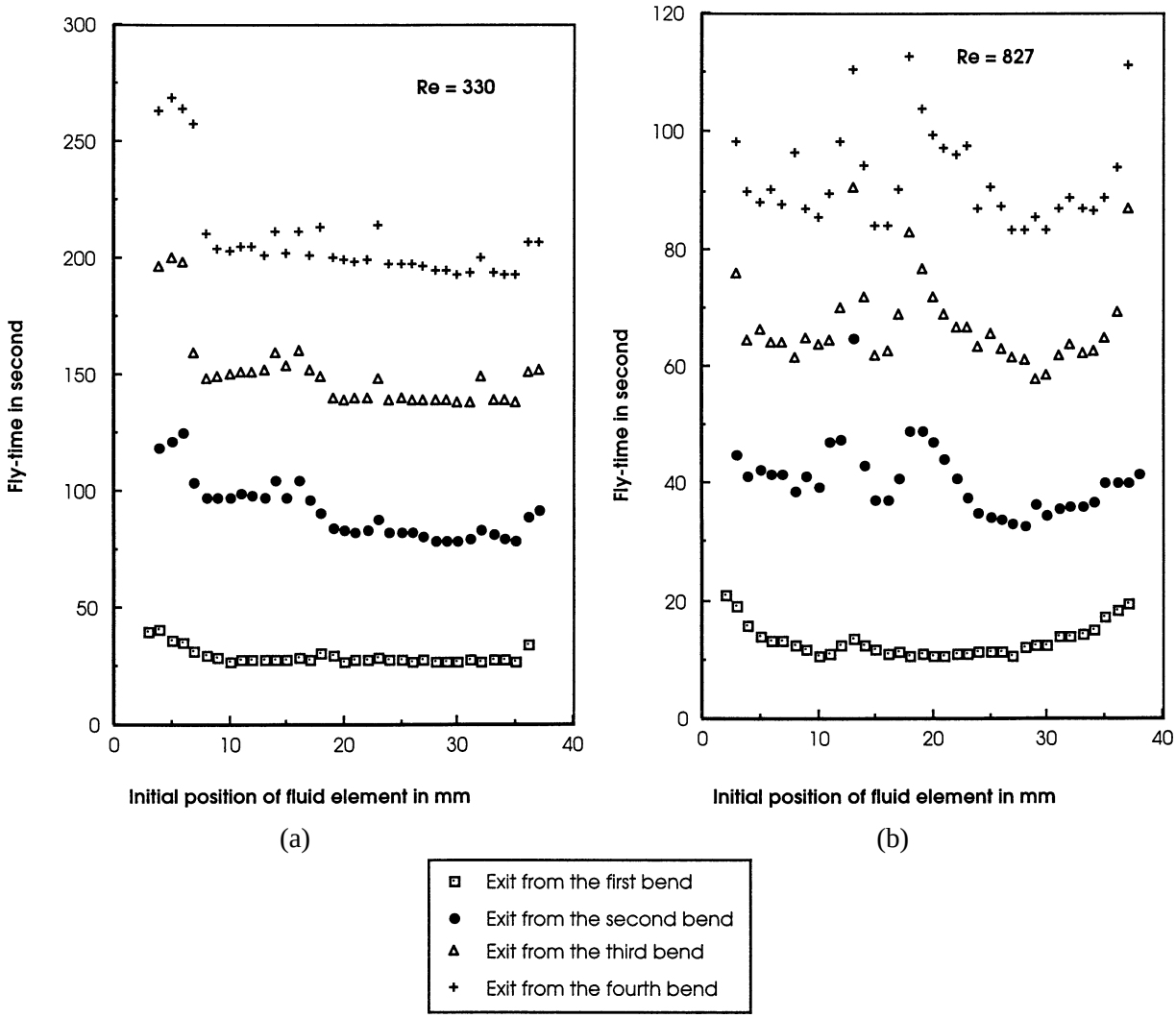

Figure 15. Experimental fly-time versus initial position of tracer blobs at the entrance to the first bend: (a) $Dn = 141$; (b) $Dn = 354$.

A low-Reynolds-number ($Re = 30$, $Dn = 10$) simulation of the flow (Mokrani et al. [22]) was performed for qualitative comparison of a regular flow (a helically coiled tube consisting of four 90° bends) with a twisted-pipe flow composed of the same number of bends arranged in a configuration similar to that of experimental situation. However, it should be noted that the simple model developed in a twisted pipe with circular cross-section does not by any means pretend to simulate the experimental case, since the square cross-section makes more complicated the modeling of the basic flow (Soh [19]). This numerical simulation is based on a simplified model developed by Jones et al. [2], which uses the approximate velocity fields for a flow in a curved pipe of circular cross-section previously developed by Dean [16]. The flow field is assumed to be steady, incompressible and fully developed in the whole geometry. Polar coordinates r, ϕ are introduced in the transverse (x, y) plane according to $x = r \sin\phi$, $y = r \cos\phi$. The velocity field is given by the following equations:

$$u = \frac{\mathrm{d}x}{\mathrm{d}t} = \frac{Dn^2}{288}\left(1 - x^2 - y^2\right)\left(4 - 5x^2 - 23y^2 + 8x^2y^2 + x^4 + 7y^4\right), \tag{2a}$$

$$v = \frac{\mathrm{d}y}{\mathrm{d}t} = \frac{Dn^2}{48}\left(1 - x^2 - y^2\right)xy\left(3 - x^2 - y^2\right), \tag{2b}$$

$$w = \frac{\mathrm{d}z}{\mathrm{d}t} = \frac{R_c\,\partial\theta}{\partial t} = \frac{Dn^2}{Re}\left(1 - x^2 - y^2\right), \tag{2c}$$

where $Re = WD/\nu$, $Dn = Re\sqrt{R/R_c}$, D the tube diameter and R the tube radius.

Since the flow is steady, the system $(u, v, w) = \left[\frac{\mathrm{d}x}{\mathrm{d}t}, \frac{\mathrm{d}y}{\mathrm{d}t}, \frac{\mathrm{d}z}{\mathrm{d}t}\right]$ is autonomous and the independent variable can be changed from time t to angular position θ by dividing equations (2a) and (2b) by equation (2c) (Jones et al. [2]). This simplification reduces the dynamical system to two equations:

$$\frac{\mathrm{d}x}{\mathrm{d}\theta} = \frac{Re}{288}\left(4 - 5x^2 - 23y^2 + 8x^2y^2 + x^4 + 7y^4\right), \tag{3a}$$

$$\frac{\mathrm{d}y}{\mathrm{d}\theta} = \frac{Re}{48}xy\left(3 - x^2 - y^2\right). \tag{3b}$$

The system of equations (3) defines the mapping of fluid particles from cross-sectional plane to another. According to Jones et al. [2], it is important to distinguish the actual time evolving advection described by (2) from the corresponding induced mapping of the cross-section given by (3).

Equations (2) satisfy the incompressibility condition in the sense that:

$$\frac{\partial x}{\partial x} + \frac{\partial y}{\partial y} = 0. \tag{4}$$

The system defined by (3), on the other hand, does not satisfy this condition. If one calculates $\frac{\partial(\mathrm{d}x/\mathrm{d}\theta)}{\partial x} + \frac{\partial(\mathrm{d}y/\mathrm{d}\theta)}{\partial y}$ it is seen to be non-zero. In this sense equation (3) leads to a mapping of the cross-section that is not area preserving. This problem can be solved if one introduces a rescaled radial coordinate R^* given by:

$$R^*(r) = r\left(1 - \frac{1}{2}r^2\right) = \sqrt{x^2 + y^2}\left(1 - \frac{1}{2}\left(x^2 + y^2\right)\right)^{1/2} \tag{5}$$

then in the (R^*, ϕ) coordinates, the mapping (3) becomes area-preserving. Details of the calculations are given in Jones et al. [2].

In a helically coiled configuration formed by the succession of n 90° bends, particle trajectories are obtained by integration of system (3) following θ between 0 and the final angular coordinate. In that procedure, torsion effects are neglected. For the chaotic case, particle trajectories are obtained by integration of system (3) between the beginning and the end of each bend. At the end of each bend, the coordinate system is changed. If the angle between the curvature plane of two successive bends is χ, the new coordinate system is obtained by a rotation $-\chi$ of the previous coordinate system corresponding to the preceding elbow.

We assume that the flow becomes fully developed as soon as it enters the bend, and that as the flow leaves one bend to enter the next, the readjustement from one secondary flow pattern to another is immediate. System (3) is numerically integrated using a fourth-order Runge–Kutta method. All the calculations have been performed in double-precision. Thanks to the simple flow model previously presented, we can calculate the trajectories of the fluid particles, in order to obtain their residence time and the cross-sectional position of each injected particle. The results are shown in *figure 16(a)*, where non-dimensional fly-times at the exit from each successive bend of a helically coiled tube for 5000 non-diffusive particles are plotted against their initial position at the

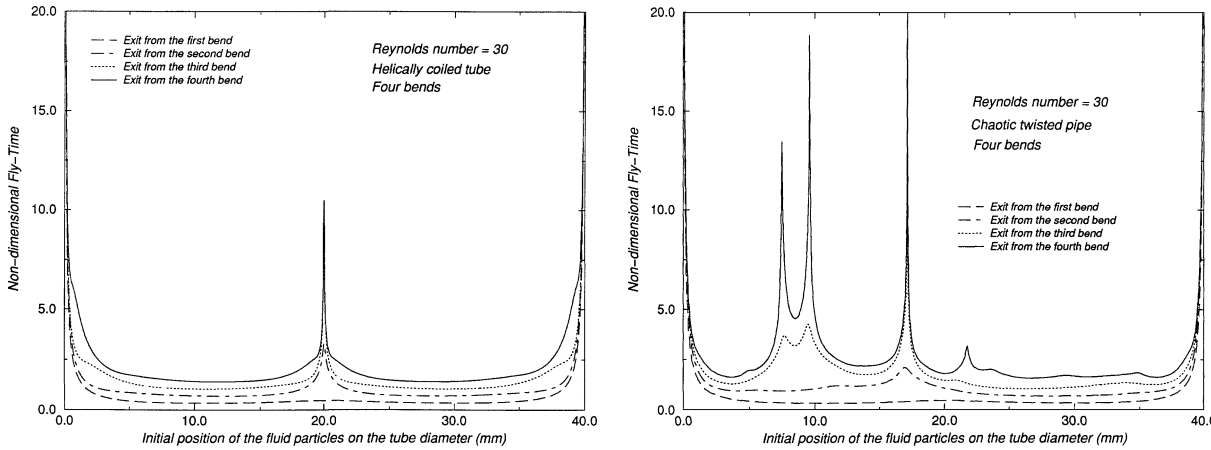

Figure 16. Numerical fly-time versus initial position of the ensemble of fluid particles at the entrance to the first bend: (a) helically coiled tube; (b) chaotic configuration.

entrance to the first bend. At the exit from the first bend, like the experimental curve, fly-time is constant for all fluid particles except those close the wall. The fly-time is also smooth everywhere at the exit from the other bends except at the center. The central peak corresponds to the fly-time of the particles located on the symmetry plane of the Dean roll-cells. As this plane is invariant in the helicoidal configuration, the fluid particles flowing on this plane are progressively retarded as they travel in the flow. *Figure 16(b)* plots fly-time for the chaotic configuration. As observed in the experiment, the fly-time is smooth at the exit from the first bend, but after the third bend, zones of irregular long fly-time start to appear. Comparison of the curves at the exit from the fourth bend in *figures 16(a), (b)* reveals the short time (local) effects of the abrupt change in curvature plane. It should be noticed, however, that what appears in *figure 16(b)* is a short-range indication of the chaotic regime. The resemblance between the curves in *figures 15* and *16(b)* suggests that the mixed state is due to the insufficient number of bends to obtain a fully chaotic regime. To attain this regime one has to wait for the asymptotic state to be reached, i.e., a large number of bends. The asymptotic state has been numerically investigated by Jones and Young [23]), who computed the angular positions reached, after a given time, by labeled particles initially distributed on a pipe diameter. Erratic chaotic zones appear in the same regions in which long fly-times have been observed in the short-time experiments equivalent to those of *figures 15* and *16(b)*.

Coexistence of regular and chaotic regimes in a flow was also observed by Kusch and Ottino [24] in a partitioned-pipe mixer; they found that this behavior is quite stable under different experimental conditions.

4.1.3. Streamline tracking observations

In this section we characterize the chaotic nature of the flow by examining the divergence of the trajectories of initially close-spaced fluid particles. To do this we selected a grid of 81 fictitious points uniformly distributed along a line in the tunnel cross-section at a distance 170 mm upstream of the entrance to the first bend. The distance between two adjacent points is 4 mm. For various Dean numbers, fluorescein tracer was injected at each point on the grid. The dye is injected one point at a time, tagging an ensemble of fluid particles initially contained in a circle of 0.25 mm diameter. The injection is continuous and smooth: each time the injector is displaced, enough time is allowed for steady state to be reestablished. The result of this experiment is 81 dispersion pictures at the exit of the fourth bend, on which we also mark the initial position of the tracer particles. *Figure 17* shows two generic cases: *figure 17(a)* corresponds to a highly dispersed case in which fluid

particles initially close to each other diverge exponentially, while *figure 17(b)* shows a poorly dispersed case in which the tagged fluid particles have been slightly displaced but stay close together.

To investigate the process leading to high or poor dispersion (corresponding to the chaotic or non-chaotic case), two specific positions of the tracer injector, namely $x/a = 0.5$, $y/a = 0.5$ and $x/a = 0.5$, $y/a = 0.75$ were selected (the coordinate origin is at the lower left corner of the cross-section). For each position a tracer filament is followed as it passes through the four bends. The Dean number for the flow in these experiments is kept at 247. Flow cross-sections were visualized by LIF and the images were recorded every 5° angular position in the flow direction (the 5° angular distance corresponds to a 19.2 mm linear distance on the twisted duct central streamline). In total, 76 flow cross-sections distributed along a 2210 mm distance in the four bends were visualized. The position with coordinates $x/a = 0.5$, $y/a = 0.5$ is among those which have shown a high dispersion of the tracer at the exit. On the other hand the position $x/a = 0.5$, $y/a = 0.75$ shows poor dispersion. For the first position, *figures 18(a)* to *(d)* superpose successive positions occupied in the cross-section plane by the tracer filament as it passes through the first, second, third and fourth bends respectively. The same images for the second injection position are shown in *figures 19(a)* to *(d)*.

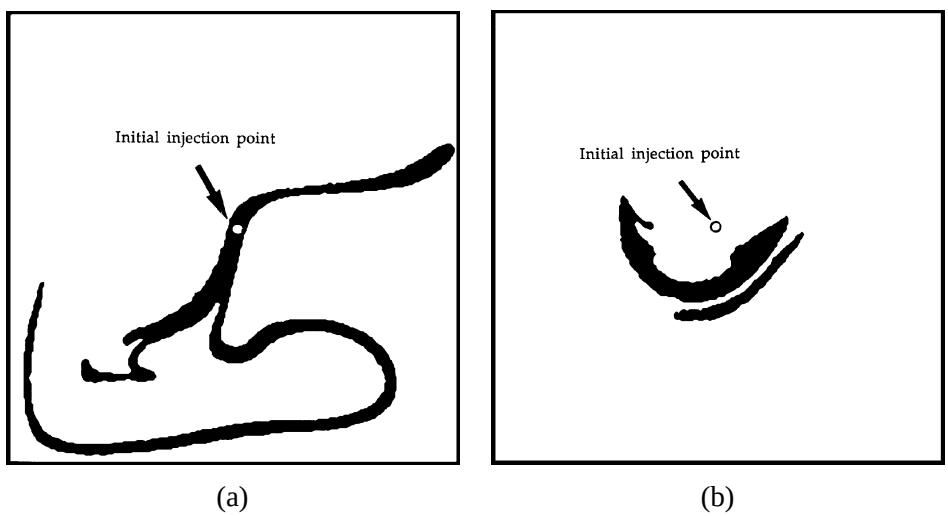

Figure 17. Visualization at the exit plane of the fourth bend of tracer streakline injected 170 mm upstream of the entrance to the first bend: (a) high-dispersion case; (b) poor-dispersion case.

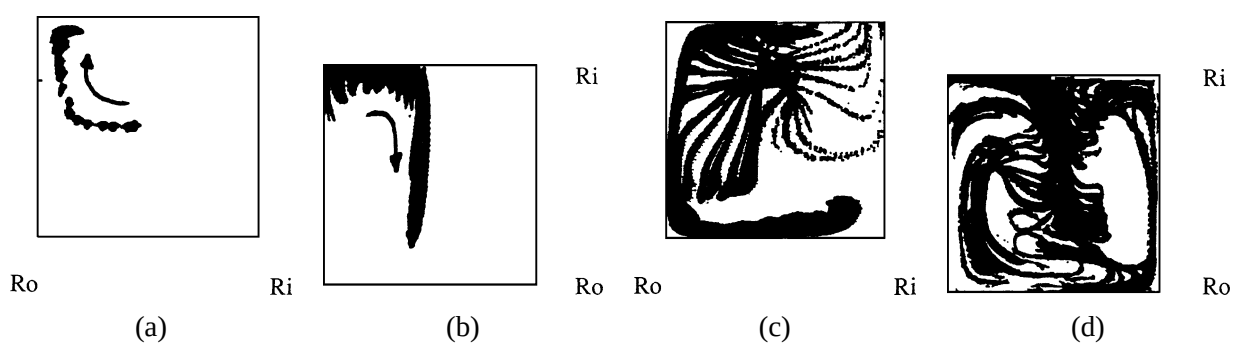

Figure 18. Superposition of 19 individual images of flow cross-section (every 5° angular position) in each bend for dye injection at namely $x/a = 0.5$, $y/a = 0.5$ at the entrance to the twisted duct: a dispersive point, $Dn = 247$ ($Re = 580$): (a) first bend; (b) second bend; (c) third bend; (d) fourth bend.

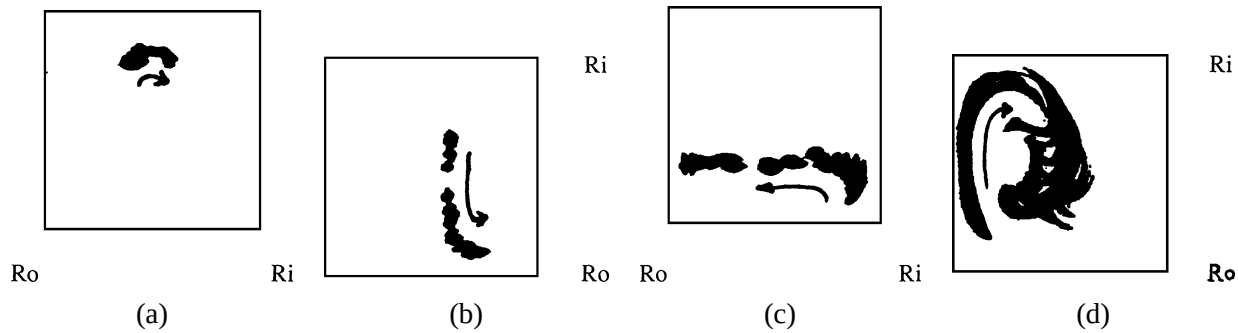

Figure 19. Superposition of 19 individual images of flow cross-section (every 5° angular position) in each bend for dye injection at $x/a = 0.5$, $y/a = 0.75$ at the entrance to the twisted duct; a poor-dispersion point, $Dn = 247$ ($Re = 580$): (a) first bend; (b) second bend; (c) third bend; (d) fourth bend.

Figures 18(a), (b) show that in the first and second bends the tagged fluid particles follow the Dean roll-cell streamlines: no important stretching or folding has occurred. On the contrary, as shown in *figure 18(c)*, the marked fluid particles are strongly stretched once they reach the stagnation point (a fixed hyperbolic point) on the concave wall (R_o) of the third bend. At this hyperbolic point, the marked fluid blob divides in two: one part is entrained by the lower Dean roll and the other part by the upper one. This stretching and dividing is repeated in the fourth bend in a direction normal to that of the third bend. Therefore a mechanism similar to baker's transformation has contributed to separating neighboring fluid particles that were initially contained in a flow tube marked by tracer at the entrance to the twisted duct.

In *figure 19*, the flow tube is initially close to an elliptic point that coincides with the center of the upper Dean roll-cell in the first bend. The successive positions of the tagged fluid particles were never in the neighborhood of a hyperbolic point, so that the stretching and dividing encountered in the previous case does not occur. This causes moderate separation of fluid trajectories, not comparable with the previous case.

4.1.4. Measurement of stretching

The flow under consideration here is three-dimensional and steady. Therefore there are three principal directions of stretching or contraction. Tracer injection is continuous, so that stretching in the axial direction cannot be investigated. Consequently, this study is limited to the measurement of transverse stretchings. In addition, stretching in the transverse direction is bounded by the duct walls.

The laser-sheet-displacement mechanism was used to illuminate the flow at intervals of 5° perpendicular to the flow direction in order to visualize the spatial evolution of the transverse dispersion of a tracer streakline. Digital image processing was used to measure the cross-sectional area and perimeter of the tracer blob (the perimeter represents the intermaterial surface between the tracer and the fluid). For this purpose a thresholding technique was used and the thresholding level was adjusted manually in some downstream positions where it was required to obtain better results. However, once an optimal level was found, for a section, the same thresholding level was applied to all images at that section, issued from different injections at the entrance to the water channel. The transverse dispersion of the tracer is a conjugated result of advection and diffusion. The molecular diffusion coefficient of fluorescein in water is $D_m = 5 \times 10^{-6}$ cm^2/s (Ramshankar and Gollub [25]). Therefore the diffusion time scale is $\tau_D = a/D_m = 3.2 \times 10^6$ seconds (= 889 hours). The time for tracer (injected at preselected points) to travel between the test section inlet and exit is $\tau = 150$ seconds. Hence the maximum transverse transport due to molecular diffusion during this time is $d = \sqrt{\tau D_m} = 0.27$ mm. This distance is negligible compared with those traveled by tracer under chaotic advection. Since the dimensions of

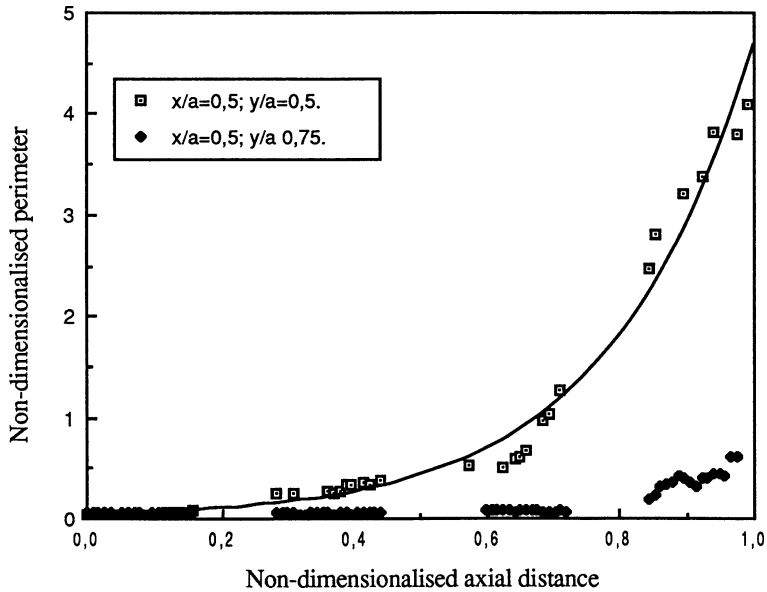

Figure 20. Streamwise evolution of the cross-section perimeter of tracer filament injected at the entrance to the first bend for a dispersive point ⊡ (exponential evolution) and a poorly dispersive point ♦ (linear evolution).

the image pixels are smaller than the transverse transport due to molecular diffusion (order of the magnitude of 110 μm), diffusion fixes the lower limit of distinguishability of two points in the flow cross-section.

The curve in *figure 20* shows the evolution of tracer cross-section perimeter with streamwise distance for injection at $x/a = 0.5$, $y/a = 0.5$ and $x/a = 0.5$, $y/a = 0.75$. The cross-section perimeter of tracer blobs is normalized by the total image perimeter. It is found that for the dispersive injection point, the perimeter grows exponentially in the space (downstream direction) according to a law of the form $P_n = P_o e^{bz}$ with $b = 4.77$. The figure also shows that the tracer follows a chaotic motion in the straight ducts between two neighboring bends. This is due to the fact that the Dean roll-cells continue to exist and to contribute to tracer transport in the straight parts of the duct. The experiment was repeated by injecting the tracer at the coordinates $x/a = 0.5$, $y/a = 0.75$. The streamwise evolution of the perimeter of the tracer cross-section is also shown in *figure 20*. Up to the exit from the third bend, the increase in the tracer perimeter is negligible. Downstream of the fourth bend, the perimeter increases linearly with streamwise distance. However, the perimeter increase is smaller than the tracer perimeter increase when the dye was injected at $x/a = 0.5$, $y/a = 0.5$. The exponent b in $P_n = P_o e^{bz}$ can be considered an equivalent of the average Lyapunov exponent for open flows: a positive b value corresponds to chaotic flow.

4.2. Evaluation of axial and transverse dispersion

Chaotic advection has particular dispersion properties. Axial dispersion was evaluated in this experiment by measuring the fly-time of the tracer blobs injected on a large number (81) of discrete points on the entrance section of the twisted duct. Fly-time is measured by a stop-watch between two laser light sheets, the first located at the entrance to the duct and perpendicular to the axial flow direction, the second fixed at the exit plane from either the first or the fourth bend. The uncertainty in fly-time measurements was evaluated for each case: for the fly-time measured in the first bend it was ± 1 second, while for the four-bend configuration it was ± 2 seconds. Fly-times in the first bend vary between 20 and 50 seconds and in the four-bend arrangement

between 106 seconds and 265 seconds. This gives at most 5% and 1% reproducibility for the two configurations, respectively. Fluorescein was chosen as the passive tracer, and the tracer injector and injection procedure are the same as those described in the previous section. For different flow rates and for each injection point we measured the time for the first appearance of tracer in the light sheet at the exit of the first bend (fly-time: t_{1ap}) and the time for the first appearance of the tracer in the light sheet at the exit of the fourth bend (fly-time: t_{4ap}). The times are non-dimensionalized by the average time t_m for a particle to travel on the central line of the twisted duct.

Figures 21(a), (b) show qualitatively the effect of chaotic advection on the axial and transverse dispersion. These figures show contour of lines of iso-values of fly-time for the one-bend and four-bend configurations, respectively. The flow Dean number is 352. *Figure 21(a)* (exit from the first bend) shows a zone of large non-dimensional (inverse) fly-time t_m/t concentrated close to the concave wall of the duct cross-section, implying the existence of a high-velocity zone in this region and low velocity everywhere else. On the other hand, *figure 21(b)* shows that high and low velocity zones are distributed in the fourth duct cross-section. This implies that fluid particles have sampled many low- and high-speed zones in the flow in such a way that at the exit their fly-time is almost uniform.

Histograms of the fly-times in one bend and four-bend flows are shown in *figure 22* for Dean numbers 141 and 352. One observes that for the one-bend flow the histograms have long tails in the low $\langle t_m/t \rangle$ corresponding to the fluid particles flowing at a speed less than that of the average speed, and also that the histograms are spread over a wide range of $\langle t_m/t \rangle$. For the four-bend flow, on the other hand, the histograms show a high concentration of non-dimensional time around an average. For $Dn = 352$ this concentration is more evident: fly-times fall into only five classes. Thus as a result of chaotic advection the velocity field is more homogenous and fluid particles pass through many different low-speed and high-speed zones in such a way that on average their fly-times are more uniform.

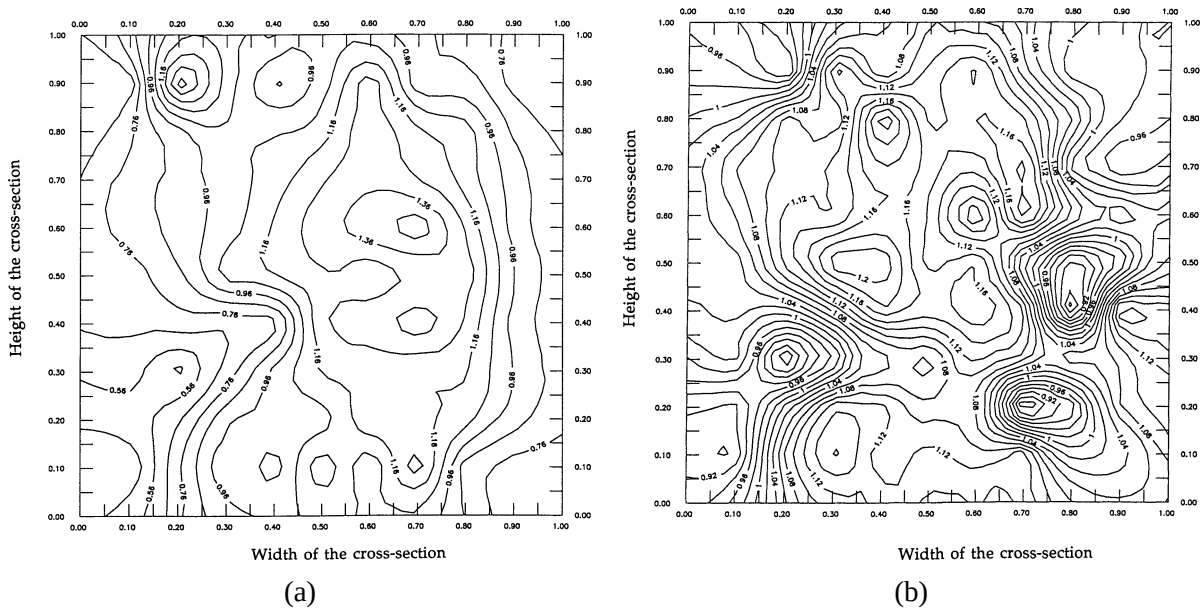

Figure 21. Contour lines of iso-values of fly-time for $Dn = 353$: (a) exit from the first bend; (b) exit from the fourth bend.

Table I shows the mean $\langle t_m/t \rangle$ and the variance σ_{ax}^2 of the non-dimensional fly-time for two Dean numbers 141 and 352 where

$$\sigma_{ax}^2 = \frac{1}{N_f} \sum_{i=1}^{N_f} (t_i - \overline{t})^2. \tag{6}$$

N_f is the number of the ensembles of fluid particles and $\overline{t}$ is the mean of t_i. One-bend and four-bend configurations are represented for each Reynolds number. It can be seen that for $Dn = 141$ the variance of the fly-time in the one-bend configuration is 4.85 times greater than that in the four-bend configuration. This ratio is 7.4 for Dean number 352.

The axial dispersion of an ensemble of fluid particles in a flow is related to the time rate of the axial variance σ_{ax}^2 of the positions of the fluid particles with respect to the center of mass of the population (Koch and Brady [26]). By replacing time with space, the axial variance of the positions of the particles is replaced by the variance of the fly-time of the particles σ_{ax}^2 for a given distance; in our specific case exit from the first or the fourth bend exit. This is the value given in *table I* (σ_{ax}^2). The large ratio of axial variances of the fly-time at the exit from the first and fourth bends shows a rapid reduction in axial dispersion due to the chaotic trajectories generated in the twisted duct. This reduction is compensated, as will be shown below, by an increase in the transverse dispersion.

To measure the increase in transverse dispersion, parallel to the fly-time measurements, the evolution of the cross-section of the tracer filament at the exit from the fourth bend was recorded. Information concerning the transverse transport of tracer was extracted from digitized images of the cross-section of tracer filaments. For each run, coordinates at the entrance (x_o, y_o) of the injection point and coordinates of the center of mass

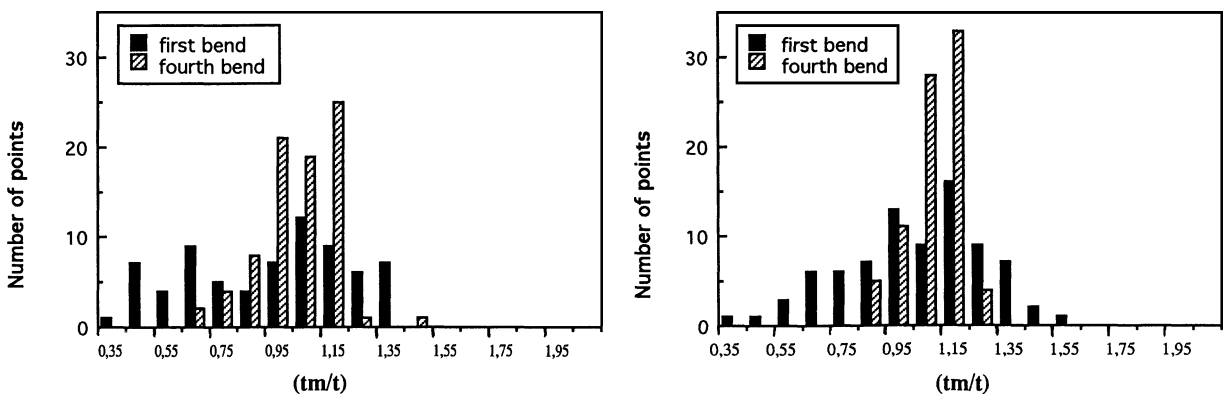

Figure 22. Histograms of non-dimensional fly-time distributions at the exit of the first and the fourth bends for different Dean numbers: (a) $Dn = 141$; (b) $Dn = 353$.

Table I. Mean time and variance of non-dimensional fly-time for two Reynolds numbers at the exit of the first and the fourth bends.

	$Re = 330$		$Re = 827$	
	Bend 1	Bend 4	Bend 1	Bend 4
$x = \langle t_m/t \rangle$	0.946	1.016	1.000	1.073
σ_{ax}^2	0.077	0.0159	0.064	0.0086
$\sigma_{ax1\text{bend}}^2/\sigma_{ax4\text{bend}}^2$	4.85		7.40	

(x_f, y_f), area a_f and perimeter P_f of the tracer blob at the exit from the fourth bend are recorded. *Figure 23* shows an example of the variation of the perimeter of the tracer blob at the exit plane from the twisted duct for $Dn = 352$, demonstrating that stretching is not produced uniformly in the flow: some regions have more capacity than others for transverse transport of tracer.

Transverse transport of tracer in two orthogonal directions x and y can be characterized by the directional variances σ_x^2 and σ_y^2 in these directions (Crisanti et al. [27]), defined as:

$$\sigma_x^2 = \frac{1}{N_f}\sum_{i=1}^{N_f}(x_i - x_{i-0})^2, \qquad \sigma_y^2 = \frac{1}{N_f}\sum_{i=1}^{N_f}(y_i - y_{i-0})^2, \tag{7}$$

where the index i labels the test particles and $i - 0$ labels the initial position of test particle i, and N_f is the number of the particle ensemble. In the case of pure diffusion that follows a Gaussian distribution, σ_x^2 and σ_y^2 vary linearly with time. In the present experiment the variances were obtained experimentally for an ensemble of 81 fluid elements marked at the entrance to the twisted duct. Hence N_f is not the number of test particles but the number of test blobs, and x_i and y_i are the coordinates of the center of mass of the blobs in local coordinates at the exit from the fourth bend. However, in order to compare the final positions of the labeled fluid with their initial positions, variances have been calculated in Lagrangian coordinates with origin at the origin of the local coordinates at the entrance to the twisted duct. *Table II* shows the values of σ_x^2, σ_y^2 and σ_{ax}^2 for Dean numbers equal to 141 and 352. Values of axial variances are at least one order of magnitude smaller than those of σ_x^2 and

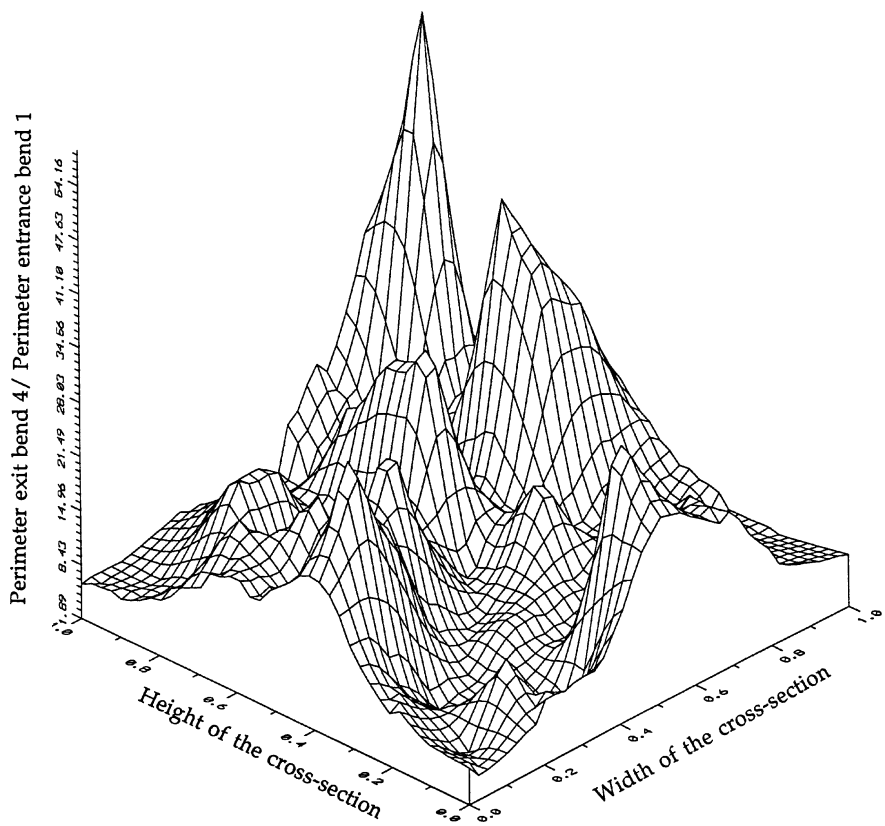

Figure 23. Variation of the non-dimensional perimeter of tracer blobs at the exit plane of the fourth bend for $Dn = 353$.

Table II. Axial and transverse dispersion for two Reynolds numbers at the exit of the first and the fourth bend.

	$Re = 330$	$Re = 827$
σ_x^2	0.126	0.095
σ_y^2	0.150	0.121
σ_{ax}^2	0.0159	0.0086

σ_y^2, implying that neighboring fluid elements at the entrance are highly separated in the transverse direction, causing a much larger transverse dispersion than reduction in axial dispersion.

5. Conclusions and discussion

Laminar flow in a twisted duct was investigated experimentally. Abrupt changes in the curvature plane at the 90° bends that constitute the duct caused fundamental changes in the flow properties, showing early signs of chaotic advection. From Eulerian point of view, the flow encountered here is a subclass of laminar flow.

The flow was investigated from the local Eulerian point of view. The axial velocity distributions in the flow cross-section were measured after each curvature change as well as at every 15° angular position in each bend. The flow enters in the twisted duct with a parabolic velocity profile. In the first bend, roll-cell development reveals the generic characteristics of a classical Dean flow. After each curvature discontinuity, the velocity distribution and roll-cell visualization showed that the flow does not adapt itself immediately to the new geometry; it rather follows the secondary flow configuration of the previous bend. In most cases it takes up to 30° for roll-cells to begin to respond to the new geometry, i.e. for the symmetry plane of roll-cells to be oriented with the curvature plane of the bend. This mechanism is invariant with the position of the bend in the twisted duct.

It is shown that the flow is sensitive to the initial conditions: neighboring fluid particles at the entrance to the twisted duct are separated exponentially at the exit from it. It has also been demonstrated that the flow produces very complex stretching and folding patterns in material lines. This would not have happened had the four bends not been arranged in such a way that the flow experiences strong torsion due to the changes in the curvature-planes of the bends. In fact, Dean roll-cells produced in the bends effect the generation of chaotic trajectories.

However, due to the small number (four) of the bends, a globally ‘mixed regime’ could be observed, i.e. islands of irregular flow emerging from a regular flow. This ‘short-range’ observation was confirmed by a numerical simulation (Mokrani et al. [22]) and was also in good agreement with the small-bend-number results of the ‘long-range’ simulation of Jones and Young [23].

The stretching was measured as a function of the streamwise coordinate in the flow direction. In the zones where irregular (chaotic) flow prevails, an exponential stretching was observed. An exponential law was proposed to describe the stretching, where the exponent can be interpreted as the equivalent of the Lyapunov exponent.

From the topological point of view, one can argue that the two stagnation points at the junction of the roll-cells symmetry plane and duct walls are hyperbolic fixed points. The symmetry streamline in the flow cross-section, in this case, becomes a heteroclinic connection.

The flow produces horseshoe-type maps by continuous stretching and folding. It is shown by fluid tagging that a material line in the flow midplane is stretched and folded so much that after only four bends it occupies a very large region of the cross-section.

The fly-time of fluid particles in the twisted duct configuration was measured for two Dean numbers. Fly-time distributions diagrams have been reconstructed and compared with that of a single bend of a quarter of a circle. Comparison between the variances of axial and transverse distribution of fly-times in the system showed that the increase (due to chaotic advection) of the variance of transverse dispersion is at least one order of magnitude larger than the decrease in the variance of axial dispersion. It has also been shown that the nondimensional fly-time distribution in the flow cross-section is much more uniform in the four-bend twisted geometry than in the one-bend geometry. This implies that the particle trajectories are irregular in such a way that they visit a large number of randomly distributed points in the flow cross-section.

References

[1] Aref H., Stirring by chaotic advection, J. Fluid Mech. 143 (1984) 1–21.
[2] Jones S.W., Thomas O.M., Aref H., Chaotic advection by laminar flow in a twisted pipe, J. Fluid Mech. 209 (1989) 335–357.
[3] Le Guer Y., Peerhossaini H., Order breaking in Dean flow, Phys. Fluids A 3 (1991) 1029–1032.
[4] Saxena A.K., Nigam K.D., Coiled configuration for flow inversion and its effect on residence time distribution, AICHE J. 30 (3) (1984) 363–368.
[5] Ottino J.M., Mixing, chaotic advection and turbulence, Annu. Rev. Fluid Mech. 22 (1990) 207–253.
[6] Villermaux E., Hulin J.P., Chaos Lagrangien et mélange de fluides visqueux, Eur. J. Phys. (1990) 179–183.
[7] Castelain C., Mokrani A., Legentilhomme P., Peerhossaini H., Residence time distribution in twisted pipe flows: helically coiled system and chaotic system, Exp. Fluids 22 (1997) 359–368.
[8] Acharya N., Sen M., Chang H.C., Heat transfer enhancement in coiled tubes by chaotic mixing, Int. J. Heat Mass Tran. 35 (10) (1992) 2475–2489.
[9] Peerhossaini H., Castelain C., Le Guer Y., Heat exchanger design based on chaotic convection, Exp. Therm. Fluid Sci. 7 (1993) 333–344.
[10] Mokrani A., Castelain C., Peerhossaini H., On the effects of chaotic advection on heat transfer, Int. J. Heat Mass Tran. 40 (13) (1997) 3089–3104.
[11] Khakhar D.V., Rising H., Ottino J.M., An analysis of chaotic mixing in two chaotic flows, J. Fluid Mech. 172 (1986) 419–451.
[12] Arnold V.I., Sur la topologie des écoulements stationnaires des fluides parfaits, C.R. Acad. Sci. Paris 261 (1965) 17–20.
[13] Khakhar D.V., Franjione J.G., Ottino J.M., A case of study of chaotic mixing in deterministic flows: the partitioned-pipe mixer, Chem. Eng. Sci. 42 (12) (1987) 2909–2926.
[14] Le Guer Y., Etude des phénomènes de transport en régime d'advection chaotique, Ph.D. Dissertation, Thermofluids and Complex Flows Research Group, LTI, ISITEM, University of Nantes, 1993.
[15] Peerhossaini H., Wesfreid J.E., Experimental study of the Taylor–Görtler instability, in: Wesfreid J.E., Brand H.R., Manneville P., Albinet G., Boccara N. (Eds.), Propagation in Systems Far from Equilibrium, Vol. 331, Springer-Verlag, 1988.
[16] Dean W.R., Note on the motion of fluid in a curved pipe, Philos. Mag. 4 (1927) 208–223.
[17] Humphrey J.A.C., Taylor A.M.K., Whitelaw J.H., Laminar flow in a square duct of strong curvature, J. Fluid Mech. 83 (3) (1977) 509–527.
[18] Duchêne C., Peerhossaini H., Michard P.J., On the velocity field and tracer patterns in a twisted duct flow, Phys. Fluids A7 (6) (1995) 1307–1317.
[19] Soh W.Y., Development of fluid flow in a curved duct of square cross-section and its fully developed dual solution, J. Fluid Mech. 188 (1988) 337–361.
[20] Hille P., Vehrenkamp R., Schultz-Dubois E.O., Development and structure of primary and secondary flow in a curved square duct, J. Fluid Mech. 151 (1985) 219–241.
[21] Doherty M.F., Ottino J.M., Chaos in deterministic systems: strange attractors, turbulence and applications in chemical engineering, Chem. Eng. Sci. 43 (2) (1988) 139–183.
[22] Mokrani A., Castelain C., Peerhossaini H., Numerical investigation of a passive particle dispersion in an alternating Dean flow, Unpublished results, 1995.
[23] Jones S.W., Young W.R., Shear dispersion and anomalous diffusion by chaotic advection, J. Fluid Mech. 11 (1994) 1–24.
[24] Kusch H.A., Ottino J.M., Experiments on mixing in continuous chaotic flows, J. Fluid Mech. 236 (1992) 319–348.
[25] Ramshankar R., Gollub J.P., Transport by capillory waves. Part II: Scalar dispersion and structure of the concentration field, Phys. Fluids A3 (5) (1991) 1344–1350.
[26] Koch D.L., Brady J.F., Dispersion in fixed beds, J. Fluid Mech. 154 (1985) 399–427.
[27] Crisanti A., Falcioni M., Provenzale A., Tanga P., Vulpiani A., Dynamics of passively advected impurities in simple two dimensional flow models, Phys. Fluids A4 (8) (1992) 1805–1820.